

Fe Abundances of Early Galaxies at $z = 9 - 12$ Derived with Deep JWST Spectra

MINAMI NAKANE,^{1,2} MASAMI OUCHI,^{3,1,4,5} KIMHIKO NAKAJIMA,³ YOSHIAKI ONO,¹ YUICHI HARIKANE,¹ YUKI ISOBE,^{6,7,8}
KEN'ICHI NOMOTO,⁵ MIHO N. ISHIGAKI,³ HIROTO YANAGISAWA,^{1,2} DAICHI KASHINO,³ NOZOMU TOMINAGA,^{3,9,10}
KOH TAKAHASHI,³ MOKA NISHIGAKI,^{4,3} YUI TAKEDA,^{4,3} AND KURIA WATANABE^{4,3}

¹*Institute for Cosmic Ray Research, The University of Tokyo, 5-1-5 Kashiwanoha, Kashiwa, Chiba 277-8582, Japan*

²*Department of Physics, Graduate School of Science, The University of Tokyo, 7-3-1 Hongo, Bunkyo, Tokyo 113-0033, Japan*

³*National Astronomical Observatory of Japan, 2-21-1 Osawa, Mitaka, Tokyo 181-8588, Japan*

⁴*Department of Astronomical Science, SOKENDAI (The Graduate University for Advanced Studies), 2-21-1 Osawa, Mitaka, Tokyo, 181-8588, Japan*

⁵*Kavli Institute for the Physics and Mathematics of the Universe (WPI), The University of Tokyo, 5-1-5 Kashiwanoha, Kashiwa, Chiba 277-8583, Japan*

⁶*Kavli Institute for Cosmology, University of Cambridge, Madingley Road, Cambridge, CB3 0HA, UK*

⁷*Cavendish Laboratory, University of Cambridge, 19 JJ Thomson Avenue, Cambridge, CB3 0HE, UK*

⁸*Waseda Research Institute for Science and Engineering, Faculty of Science and Engineering, Waseda University, 3-4-1, Okubo, Shinjuku, Tokyo 169-8555, Japan*

⁹*Astronomical Science Program, Graduate Institute for Advanced Studies, SOKENDAI, 2-21-1 Osawa, Mitaka, Tokyo 181-8588, Japan*

¹⁰*Department of Physics, Faculty of Science and Engineering, Konan University, 8-9-1 Okamoto, Kobe, Hyogo 658-8501, Japan*

ABSTRACT

We derive Fe-abundance ratios of 6 galaxies at $z = 9 - 12$ with $-22 < M_{\text{UV}} < -19$ whose JWST/NIRSpec spectra achieve very high signal-to-noise ratios, $\text{SNR} = 40 - 230$, at the rest-frame UV wavelength. We fit stellar synthesis model spectra to these JWST spectra, carefully masking out nebular emission, interstellar absorption, and non-iron stellar absorption lines, and obtain Fe-abundance ratios of $[\text{Fe}/\text{H}] = -2 - 0$ for 4 galaxies and upper limits of $[\text{Fe}/\text{H}] \sim -1$ for 2 galaxies. We compare these $[\text{Fe}/\text{H}]$ values with the oxygen abundances of these galaxies ($7.2 < 12 + \log(\text{O}/\text{H}) < 7.9$) in the same manner as previous studies of low- z galaxies, and derive oxygen-to-iron abundance ratios $[\text{O}/\text{Fe}]$. We find that majority of (4 out of 6) galaxies are consistent with iron-poor abundance ratios ($[\text{O}/\text{Fe}] \gtrsim 0$) while that 2 out of 6 galaxies, GS-z11-0 and GN-z11, show Fe enhancements ($[\text{O}/\text{Fe}] < 0$), especially GS-z11-0 ($z = 11.12$) with a Fe enhancement ($[\text{O}/\text{Fe}] = -0.91^{+0.35}_{-0.42}$) beyond the solar-abundance ratio at $\sim 3\sigma$. Because, unlike GS-z11-0, GN-z11 ($z = 10.60$) may be an AGN, we constrain $[\text{O}/\text{Fe}]$ via FeII emission under the assumption of AGN and confirm that the Fe enhancement is consistent even in the case of AGN. While $[\text{O}/\text{Fe}]$ values of the majority of the galaxies are explained by the chemical enrichment of core-collapse supernovae (CCSNe), the Fe enhancements of GS-z11-0 and GN-z11 are puzzling. We develop chemical evolution models, and find that the iron enhancements against oxygen in GS-z11-0 and GN-z11 can be explained by 1) pair-instability supernovae/bright hypernovae with little contribution of CCSNe or 2) Type-Ia supernovae with short delay time ($\sim 30 - 50$ Myr) with a top-light initial mass function.

Keywords: Galaxy chemical evolution (580); Galaxy evolution (594); Galaxy formation (595); High-redshift galaxies (734); Star formation (1596)

1. INTRODUCTION

The chemical enrichment of galaxies caused by stellar nucleosynthesis and supernovae provides the insight into star formation of the galaxies. The high sensitivity of the Near Infrared Spectrograph (NIRSpec; Jakobsen et al. 2022) of the James Webb Space Telescope (JWST;

Gardner et al. 2023) allows us to measure the various chemical abundance ratios of galaxies at $z \sim 4 - 14$ from emission lines: O/H (e.g., Curti et al. 2023; Nakajima et al. 2023; Sanders et al. 2024), C/O (e.g., Arellano-Córdova et al. 2022; Isobe et al. 2023b; D'Eugenio et al. 2024a), N/O (e.g., Cameron et al. 2023; Isobe et al.

2023b; Castellano et al. 2024; Topping et al. 2024a,b), and Ne/O (e.g., Arellano-Córdova et al. 2022; Isobe et al. 2023b). In massive stars, these elements are produced in the outer to intermediate layers via the nuclear fusion reactions (e.g., Nomoto et al. 2013). However, abundances of Fe, which is produced in the innermost regions of the massive stars, are investigated for only a few high- z galaxies, such as GS_3073 ($z = 5.55$; Ji et al. 2024a), GS 9422 ($z = 5.94$; Tacchella et al. 2024), and GN-z11 ($z = 10.60$; Ji et al. 2024b; Nakane et al. 2024) due to weak Fe emission lines.

For star-forming galaxies at $z = 2 - 6$, iron abundances are measured from spectral fitting including UV stellar absorption lines of iron (e.g., Rix et al. 2004) with stellar synthesis model spectra (Steidel et al. 2016; Cullen et al. 2019; Harikane et al. 2020; Cullen et al. 2021; Kashino et al. 2022). Nakane et al. (2024) obtain the abundance ratio of [O/Fe] for GN-z11 at $z = 10.60$, with the iron abundance derived with the same spectral fitting method and the oxygen abundance measured from the emission lines. The resulting ratio of [O/Fe] = $-0.37^{+0.43}_{-0.22}$ is lower than the ones of the star-forming galaxies at $z = 2 - 6$ ([O/Fe] $\sim 0.3 - 0.6$; Steidel et al. 2016; Cullen et al. 2019; Harikane et al. 2020; Cullen et al. 2021; Kashino et al. 2022) and Milky Way (MW) stars ([O/Fe] $\sim -0.2 - 0.7$; e.g., Bensby et al. 2013), implying iron enhancement in the early epoch only 430 Myr after the Big Bang.

In the MW stars, [O/Fe] ratios are high at low [Fe/H] and low at high [Fe/H], which is explained with core-collapse supernovae (CCSNe) and Type-Ia supernovae (SNe Ia) (e.g., Suzuki & Maeda 2018). This is because iron enhancement is normally caused by SNe Ia, which occur later than instantaneous CCSNe due to the delay time (typically $\sim 0.1 - 1.0$ Gyr) for the white dwarf formation and gas accretion/white dwarf merger. In the case of GN-z11, however, such early enhancement of iron by SNe Ia is difficult unless the delay times is very short, and other possibilities of bright hypernovae (BrHNe; e.g., Umeda & Nomoto 2008; Leung & Nomoto 2024) and/or theoretical pair-instability supernovae (PISNe; e.g., Takahashi et al. 2018), which eject a lot of iron due to the high explosion energies and high mass cut, are also suggested (Nakane et al. 2024). In similar cases, the observed low O/Fe ratios of extremely metal poor galaxies (EMPGs) in the local Universe, which are very young (\sim a few tens of Myr), suggest the Fe enhancement by BrHNe/PISNe or SNe Ia with short delay time (Kojima et al. 2021; Isobe et al. 2022; Watanabe et al. 2024).

In this study, we investigate iron abundances of 6 galaxies at $z \sim 9 - 12$ using NIRSpec deep spectra

observed in the multiple programs to explore the processes of iron enrichment of high- z galaxies with a larger sample. This paper is organized as follows. Section 2 describes the NIRSpec data obtained from the multiple programs and defines our sample of galaxies at $z \sim 9 - 12$. In Section 3, we measure iron abundances with the spectral fitting and oxygen abundances with the nebular emission lines, and present the resulting [O/Fe] ratios of our sample galaxies. In Section 4, we construct the chemical evolution models including CC-SNe, SNeIa, and PISNe, and discuss the origins of the iron enhancement in the early epoch of the Universe. Section 5 summarizes our findings. We assume a standard Λ CDM cosmology with $\Omega_\Lambda = 0.7$, $\Omega_m = 0.3$, and $H_0 = 70 \text{ km s}^{-1} \text{ Mpc}^{-1}$. All magnitudes are in the AB system (Oke & Gunn 1983). Throughout this paper, we utilize the solar abundance ratios of Asplund et al. (2021). The notation [X/Y] is defined as $\log(X/Y)$ subtracted by the solar abundance ratio of $\log(X/Y)_\odot$.

2. DATA AND SAMPLE

2.1. NIRSpec Spectra

The spectroscopic data used in this study were obtained with NIRSpec in multiple programs of the public observations; the Cosmic Evolution Early Release Science (CEERS; ERS-1345, PI: S. Finkelstein; Finkelstein et al. 2023, Arrabal Haro et al. 2023a), the Director’s Discretionary Time (DDT) observations (DDT-2750, PI: P. Arrabal Haro; Arrabal Haro et al. 2023b), the General Observer (GO) observations (GO-1433, PI: D. Coe; Hsiao et al. 2023 and GO-3073, PI: M. Castellano), the Ultra-deep NIRCам and NIRSpec Observations Before the Epoch of Reionization (UNCOVER; GO-2561, PI: I. Labbe & R. Bezanson; Bezanson et al. 2024), and the Guaranteed Time Observations (GTO) of the JWST Advanced Deep Extragalactic Survey (JADES; GTO-1180, GTO-1181, PI: D. Eisenstein, GTO-1210, PI: N. Lützgendorf, GO-3215, PI: D. Eisenstein & R. Maiolino; Eisenstein et al. 2023a,b; Bunker et al. 2024; D’Eugenio et al. 2024b). All of the NIRSpec observations were conducted with the MOS mode using MSA. We use low resolution ($R \sim 100$) prism data that cover $0.6 - 5.3 \mu\text{m}$ because the continua, which are crucial for measuring Fe abundances (see Section 3.1), are detected clearly in the prism spectra compared to the medium-resolution ($R \sim 1000$) and high-resolution ($R \sim 2700$) grating spectra. For GN-z11, which is observed in JADES GTO-1181, we also utilize the data observed with the medium-resolution filter-grating pairs of F070LP-G140M, F170LP-G235M, and F290LP-G395M covering the wavelength of $0.7 - 1.3$, $1.7 - 3.1$, and $2.9 - 5.1 \mu\text{m}$, respectively. This is because the grat-

ing spectra allow us to measure the Mg $\lambda\lambda 2796, 2803$ lines, which is used to measure Fe abundances with active galactic nuclei (AGN) models (see Section 3.1.2), more exactly than the prism spectra. The CEERS data were taken at 8 pointing positions with the prism. The total exposure time of the CEERS data is 0.86 hours per pointing. The GO-1433 and DDT-2750 observations, each at a single pointing, were conducted with the prism, and the total exposure times are 3.7 and 5.1 hours, respectively. The GO-3073 observations were performed at 2 pointings with the prism. The exposure time is 1.8 hours for each pointing. The UNCOVER data were taken at 7 MSA mask configurations with the prism. The exposure time is 2.8 hours for each configuration. The JADES data were obtained in the multiple programs of GTO-1180, GTO-1181, GTO-1210, and GO-3215. GTO-1180 and GTO-1181 have observed 9 pointings with the prism and 3 medium-resolution gratings of F070LP-G140M, F170LP-G235M, and F290LP-G395M. The exposure times for each pointing of GTO-1180 are 1.1–3.1 hours for the prism. Each pointing of GTO-1181 is observed with the total exposure times of 1.8–2.6 and 0.9–2.6 hours for the prism and each grating, respectively. Both of the GTO-1210 and GO-3215 data were observed at 1 pointing positions with the prism. The total exposure times are 27.8 hours for GTO-1210 and 46.7 hours for GO-3215.

2.2. Data Reduction

We have reduced the GO-3073 data in the same way as Nakajima et al. (2023) and Harikane et al. (2024). We have extracted the raw data from the Mikulski Archive for Space Telescopes (MAST) archive and performed level-2 and -3 calibrations using the JWST pipelines (ver.1.16.0) with the Calibration Reference Data System (CRDS) context file of `jwst_1298.pmap`. We have obtained noise spectra from readout noise and Poisson noise. We use the spectroscopic redshifts of the objects measured from the nebular emission lines and Lyman break features by Castellano et al. (2024) and Napolitano et al. (2024).

The CEERS, GO-1433, and DDT-2750 data have been reduced by Nakajima et al. (2023) and Harikane et al. (2024) with the JWST pipeline version 1.8.5 with the CRDS context file of `jwst_1028.pmap` or `jwst_1027.pmap` with additional processes improving the flux calibration, noise estimate, and the composition. Nakajima et al. (2023) and Harikane et al. (2024) have measured spectroscopic redshifts z_{spec} with optical emission lines (H β and [O III] $\lambda\lambda 4959, 5007$). The

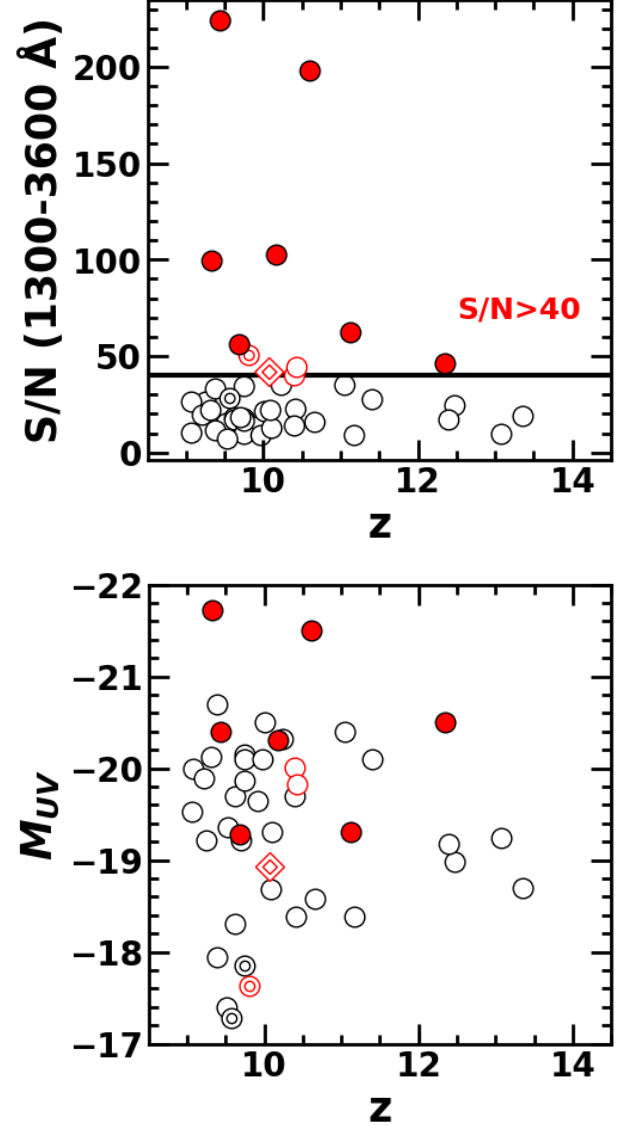


Figure 1. Top: Signal-to-noise ratio around 1300 – 3600 Å as a function of redshift. The red-filled circles represent our sample galaxies with $S/N(1300 - 3600 \text{ Å}) > 40$. The red open circles (diamond) denote the galaxies with $S/N(1300 - 3600 \text{ Å}) > 40$ which we do not select due to the lack of sufficient emission lines for oxygen abundance measurements (X-ray detection as a strong signature of AGN; Goulding et al. 2023; Bogdán et al. 2024). The black open circles show the galaxies with $S/N(1300 - 3600 \text{ Å}) \leq 40$. The double circles (diamond) indicate the lensed galaxies whose magnification factors are $\mu > 5$. The black solid line presents the criteria of $S/N(1300 - 3600 \text{ Å}) = 40$ for selecting the our sample galaxies. Bottom: Absolute UV magnitude distribution as a function of redshift. The symbols are the same as in the top panel.

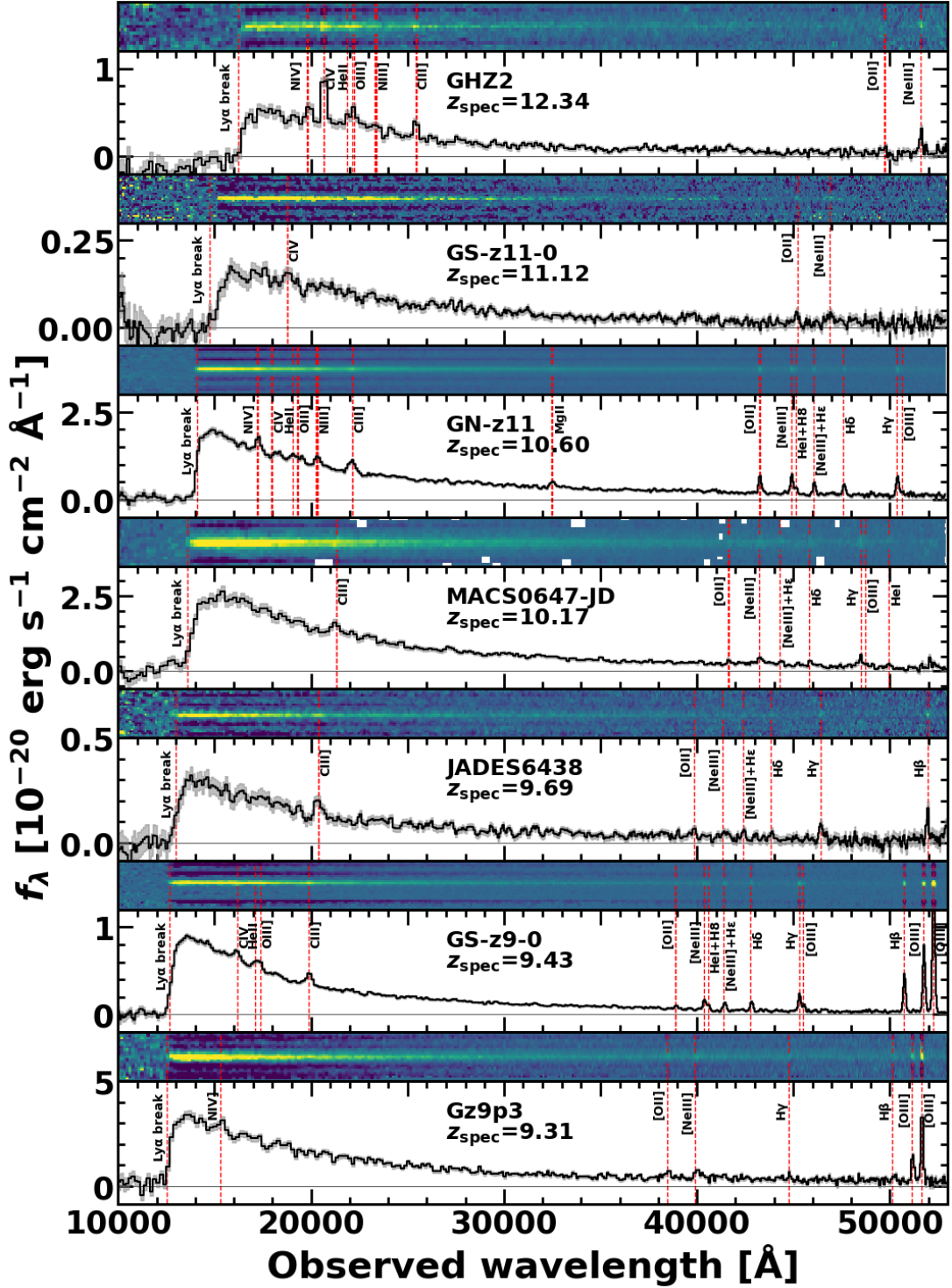


Figure 2. Spectra of the 7 galaxies in our sample. Each panel shows the two-dimensional spectrum (top) and the one-dimensional spectrum (bottom). The black solid lines and shaded regions represent the observed spectra and their 1σ uncertainties, respectively. The red dashed lines indicate Lyman break features and other emission lines.

JADES data are publicly available¹, and have already been reduced with the pipeline developed by the ESA NIRSpec Science Operations Team and the NIRSpec GTO Team. The redshifts are spectroscopically measured by Bunker et al. (2024) and D'Eugenio et al. (2024b) with the emission lines (e.g., $H\beta$ and $[O\ III]\ \lambda\lambda 4959, 5007$) or Lyman breaks. The UNCOVER data are publicly available² and have been reduced by Price et al. (2024). The redshifts of the galaxies at $z > 9$ are spectroscopically measured by Fujimoto et al. (2023) based on the emission lines and Lyman break features.

2.3. Sample

For iron abundance measurements, we select high-redshift galaxies whose continua are detected at high signal-to-noise (S/N) ratios with the prism. We first have collected a total of 44 galaxies at $z > 9$ from the CEERS, GO-1433, GO-3073, UNCOVER, DDT-2750, and JADES data, combined with the data from DAWN JWST Archive (DJA). For the DJA data, we only use the prism spectra with the grade 3, which are robust based on the visual inspection. We then measure S/N ratios in the rest-frame wavelength range of $1300 - 3600\ \text{\AA}$, $S/N(1300 - 3600\ \text{\AA})$, which is used to derive $[Fe/H]$ (see Section 3.1.1). In Figure 1, we present $S/N(1300 - 3600\ \text{\AA})$ and absolute UV magnitudes (M_{UV}) as a function of redshift for the 44 galaxies. We select individual 7 out of 44 galaxies whose spectra show $S/N(1300 - 3600\ \text{\AA}) > 40$, corresponding to $S/N \gtrsim 3$ per pixel of the spectra and sufficient emission lines to measure the abundance ratios of O/H (see Section 3.2). We do not include one galaxy, which is reported to be a X-ray luminous AGN (Goulding et al. 2023; Bogdán et al. 2024). The 7 galaxies with $S/N(1300 - 3600\ \text{\AA}) > 40$ are summarized in Table 1. We show the spectra of the 7 galaxies in Figure 2. Note that for GN-z11 in our sample, we use the measurements of $[Fe/H]$ and $[O/Fe]$ in the stellar case (Section 3.1.1) from Nakane et al. (2024).

3. CHEMICAL ABUNDANCES

3.1. Iron Abundance Measurement

3.1.1. Stellar Population Synthesis Spectrum Fitting

In this section, we estimate iron abundances of $[Fe/H]$, assuming that the UV radiation of the galaxies are dominated by stellar components. We conduct spectral fitting with stellar models in the same way as Nakane et al. (2024), following the studies of low- z galaxies ($z \sim 2 - 6$; Steidel et al. 2016; Cullen et al. 2019; Harikane et al.

2020; Cullen et al. 2021; Kashino et al. 2022). This method is based on the UV spectra, which are sensitive to the iron abundances of the massive young stars. This is because the UV stellar absorption features (e.g., 1370, 1425, and 1978 indices; Rix et al. 2004) are mainly due to transitions of highly ionized iron (Dean & Bruhweiler 1985; Brandt et al. 1998). The stellar model spectra consist of the stellar and nebular spectra, reddened by the dust extinction and attenuated by the intergalactic medium (IGM) absorption. For the stellar spectra, we use the population synthesis code BPASS v2.2.1 (Eldridge et al. 2017; Stanway & Eldridge 2018). We adopt the Salpeter (1955) initial mass function (IMF), of which slope is $\alpha = 2.35$, with a high-mass cutoff of $100 M_{\odot}$ including binary stars, and constant/bursty star formation history, varying stellar metallicities and ages. We also use the IMF with slope $\alpha = 2.0$ and 2.7 in the mass range of $M > 0.5 M_{\odot}$ for comparison. We calculate the nebular spectra by the photoionization code CLOUDY v23.01 (Ferland et al. 1998; Gunasekera et al. 2023), adopting the BPASS spectra as the incident spectra, a plane-parallel geometry, unity for a covering factor, an ionization parameter of $\log(U) = -2.0$ (e.g., Bunker et al. 2023; Castellano et al. 2024), and a density of $n_H = 300\ \text{cm}^{-2}$ (e.g., Steidel et al. 2016). Although recent JWST studies report the high electron densities of $n_e \sim 1000\ \text{cm}^{-3}$ for galaxies at $z \gtrsim 9$ (e.g., Isobe et al. 2023a; Abdurro'uf et al. 2024; Topping et al. 2025), Nakane et al. (2024) confirm that changing the density to $n_H = 1000\ \text{cm}^{-3}$ have little effect on $[Fe/H]$ measurements. We utilize Calzetti et al. (2000) extinction law and the IGM absorption models of Inoue et al. (2014). The stellar model spectra are smoothed to match the observed resolutions of $R = 100$ for the prism spectra.

In Figure 3, we compare the stellar model spectra for different values of $[Fe/H]$, stellar age, dust extinction, and IMF. Although the spectra with larger stellar age is reddened like those with higher $[Fe/H]$, the change of the stellar age cannot make the spectral shape similar to the one of $[Fe/H]$ due to the limitation by the cosmic age ($\sim 400 - 500\ \text{Myr}$), when the galaxies at $z \sim 9 - 12$ exist (top panel). The larger dust extinction flattens the spectra, resulting in the different spectral shape from those with high $[Fe/H]$ (middle panel). The different IMFs (i.e., slope α) have much less effects on the spectra than $[Fe/H]$, stellar age, and dust extinction (bottom panel). In addition, as mentioned above, the spectra with higher $[Fe/H]$ show the stronger stellar absorption features, which locally appear in the wavelengths where Fe absorptions exist (e.g., Figure 2 in Nakane et al. 2024). We can thus determine $[Fe/H]$

¹ <https://archive.stsci.edu/hlsp/jades>

² <https://jwst-uncover.github.io/#>

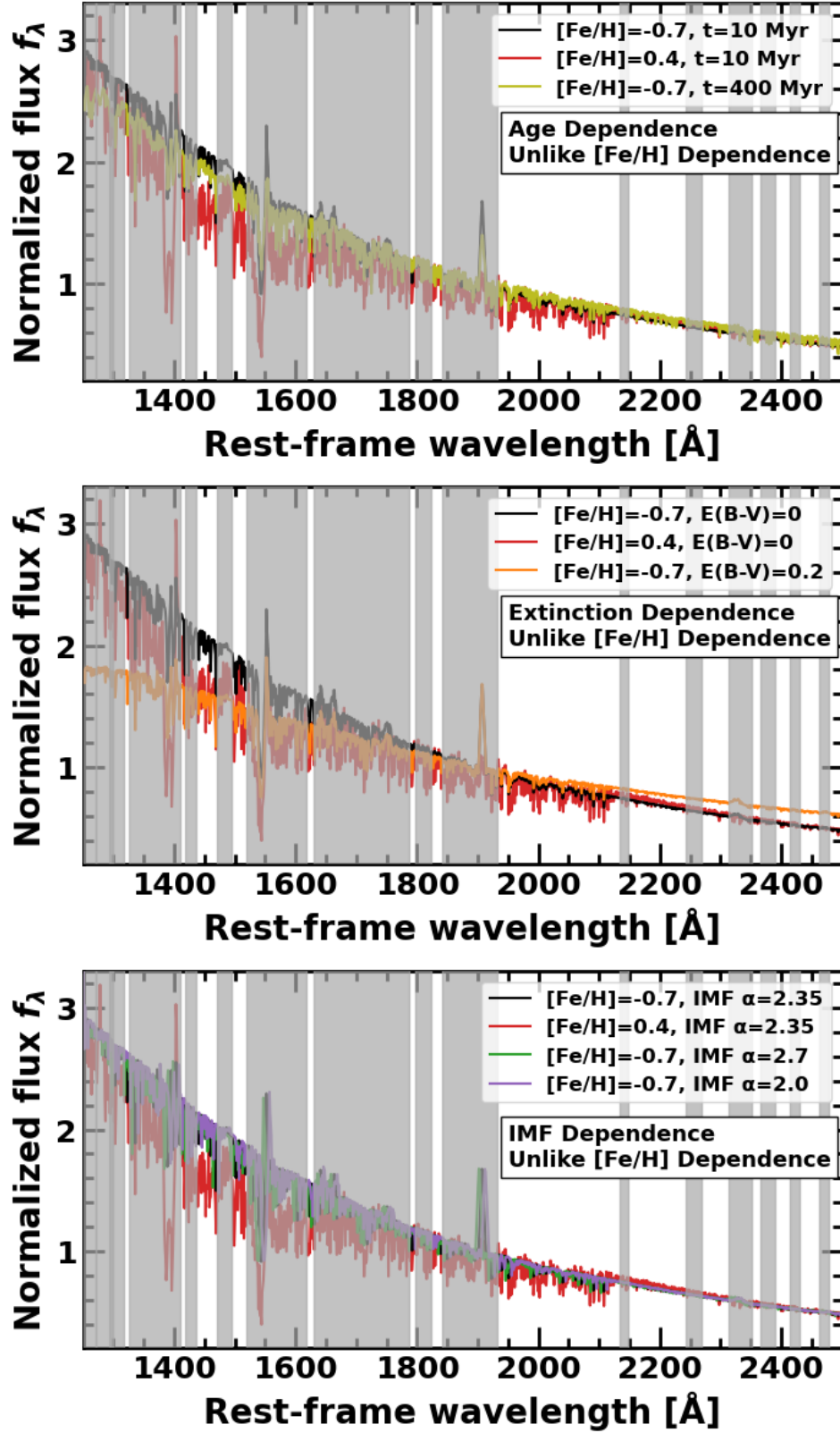


Figure 3. Comparison of the stellar model spectra. Three panels show the differences in the spectra with respect to $[\text{Fe}/\text{H}]$ and the following factors: stellar age (top), dust extinction (middle) and IMF (bottom). The black lines represent the models with $[\text{Fe}/\text{H}] = -0.7$, $t = 10$ Myr, $E(B - V) = 0$, and a [Salpeter \(1955\)](#) IMF ($\alpha = 2.35$). The red, yellow, orange, green, and purple lines indicate the same models as the black lines but for $[\text{Fe}/\text{H}] = 0.4$, $t = 400$ Myr, $E(B - V) = 0.2$, an IMF with $\alpha = 2.7$, and an IMF with $\alpha = 2.0$, respectively. For display purposes, the green and purple lines are shifted by -5 and $+5$ \AA in the x -axis, respectively. The gray-shaded regions show the wavelength regions excluded from the spectral fitting to avoid the impacts of nebular emission, interstellar absorption, and non-iron stellar absorption lines. The age change cannot make the spectral shape similar to the one of $[\text{Fe}/\text{H}]$ change (top). The extinction change flattens the spectra, which are totally different from the ones of $[\text{Fe}/\text{H}]$ change (middle). The IMF change cannot make the differences as large as the $[\text{Fe}/\text{H}]$ change (bottom).

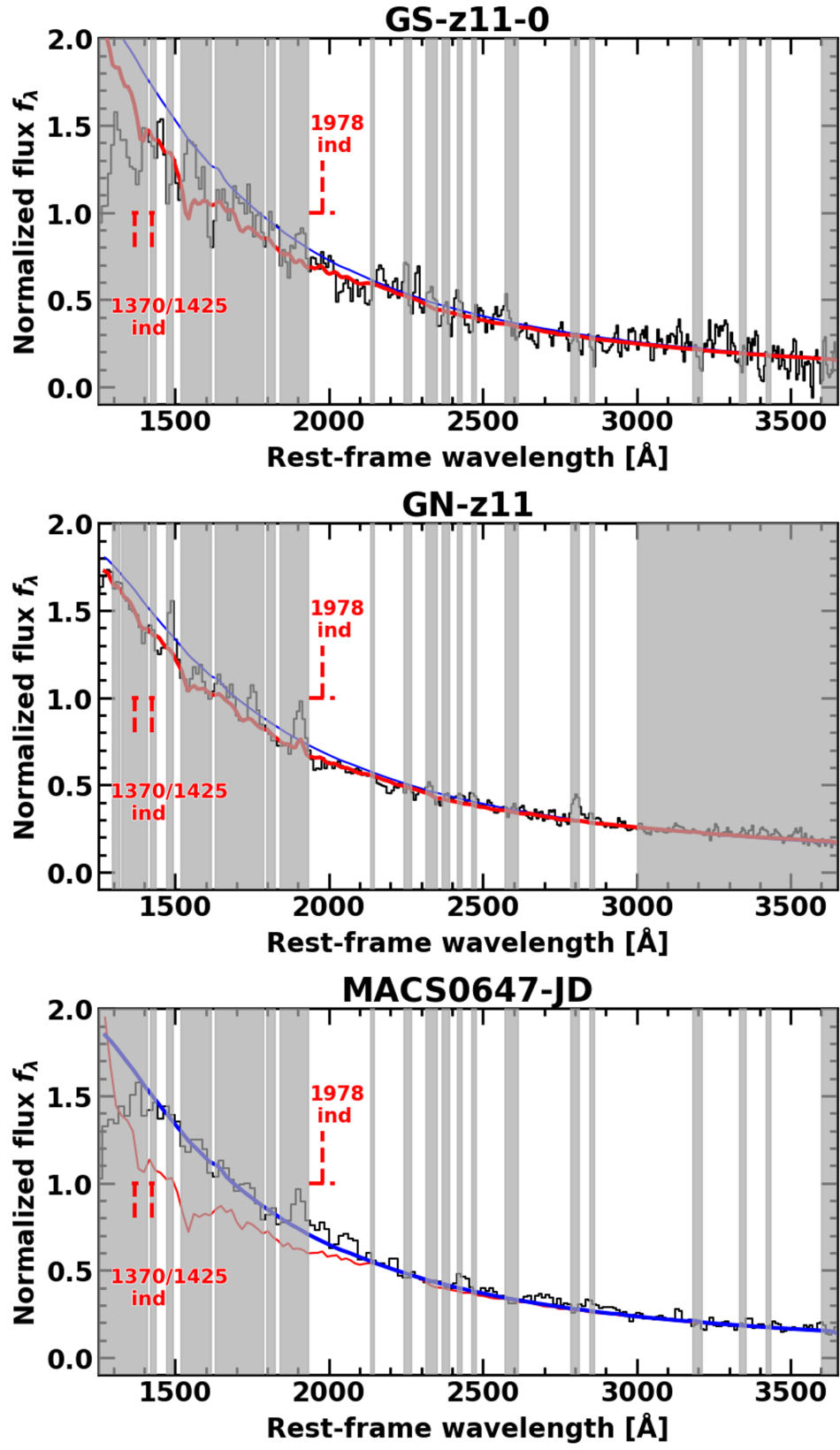


Figure 4. Comparison of the observed prism spectra and stellar model spectra for the case of high $[\text{Fe}/\text{H}]$ for GS-z11-0 (top) and GN-z11 (middle) and low $[\text{Fe}/\text{H}]$ for MACS0647-JD (bottom). The results of GN-z11 are taken from Nakane et al. (2024). The black lines show the observed prism spectra. The gray-shaded regions indicate the same as in Figure 3. The red lines denote the models with Fe-enhanced ratios of $[\text{Fe}/\text{H}] = 0.00$ (top), -0.50 (middle), and 0.40 (bottom). The blue lines represent the models with Fe-poor ratios of $[\text{Fe}/\text{H}] = -3.15$ (top), -3.15 (middle), and -3.09 (bottom). The thick lines present the best-fit models.

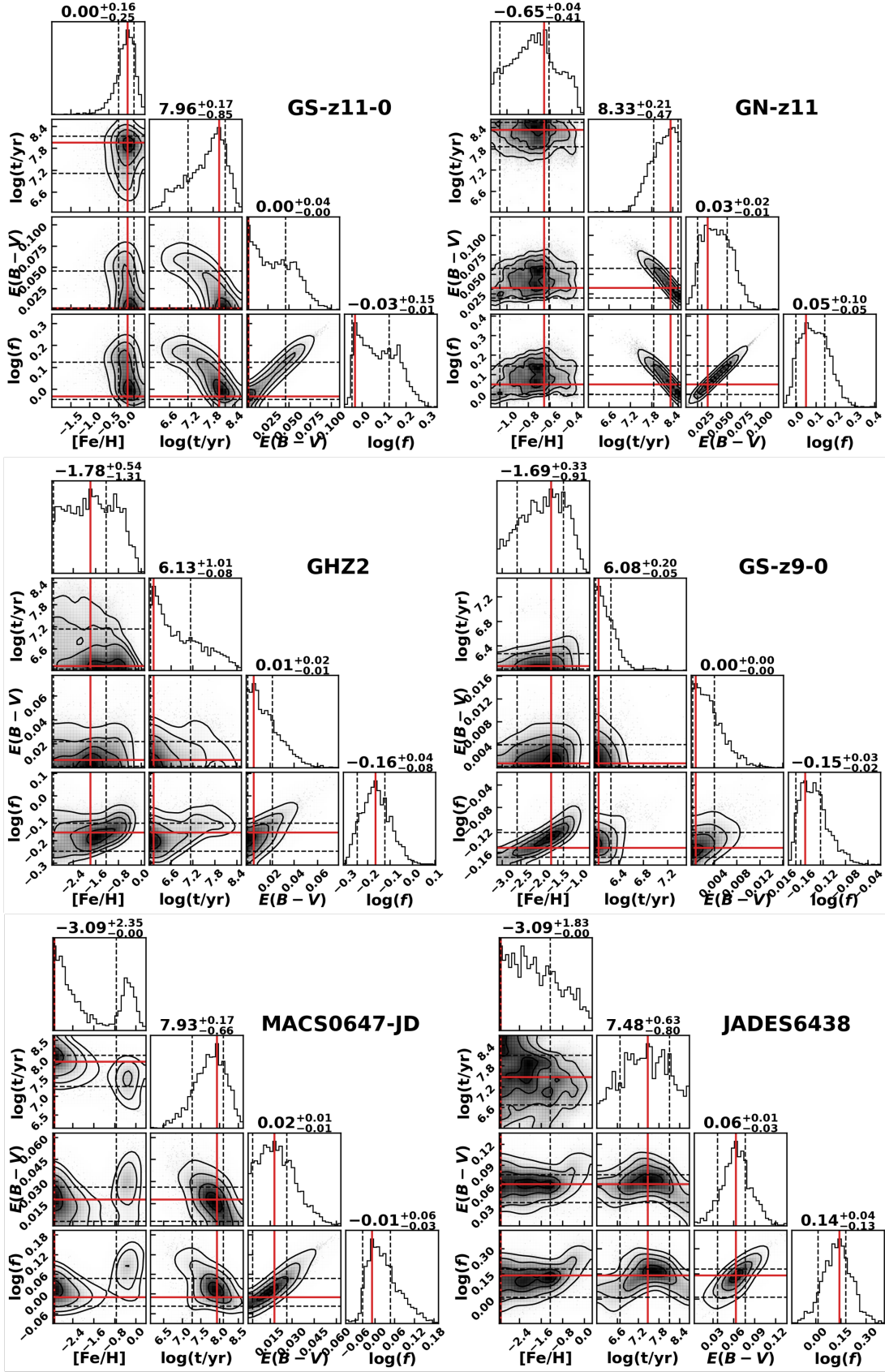


Figure 5. Posterior PDFs of the fitting parameters for our sample galaxies with the stellar model spectra. Top, middle, and bottom panels represent the results for high $[\text{Fe}/\text{H}]$, low $[\text{Fe}/\text{H}]$ and upper limits of $[\text{Fe}/\text{H}]$, respectively. For GN-z11 in the top right panel, we show the PDF obtained from the prism spectra (Nakane et al. 2024). For GN-z11 in the top left panel, The red solid lines and black-dashed lines indicate the mode and the boundaries of the 68th percentile HPDI, respectively (Section 3.1.1).

independently of the stellar age, dust extinction, and IMF, from the spectral fitting using the stellar models.

We fit the stellar model spectra to the prism spectra in the wavelength range of $1300 - 3600 \text{ \AA}$ to avoid the impacts of $\text{Ly}\alpha$ damping wing and Balmer absorption. To derive stellar metallicities, we first exclude the wavelength regions where the stellar continuum is impacted by nebular emission lines and interstellar absorption lines. We also mask out wavelengths affected by non-iron stellar absorption lines (e.g., C, O) because the stellar model spectra assume a solar abundance pattern, which enables us to consider the stellar metallicities of $\log(Z_*/Z_\odot)$ as iron abundances of $[\text{Fe}/\text{H}]$. We estimate four free parameters, the iron abundance $[\text{Fe}/\text{H}]$, stellar age t , color excess $E(B-V)$, and normalization factor of the stellar model spectra f . To obtain the posterior probability distributions functions (PDFs) of the free parameters, we perform Markov Chain Monte Carlo (MCMC) simulations with the *emcee* (Foreman-Mackey et al. 2013). We utilize flat priors of $-3.15 \leq [\text{Fe}/\text{H}] \leq 0.45$, $6.00 \leq \log(t/\text{yr}) \leq t_C$, $0.0 \leq E(B-V) \leq 1.0$, and $-2.0 \leq \log(f) \leq 2.0$, where t_C is the cosmic age corresponding to the redshift of the galaxy. We determine the free parameter from the mode (i.e., a peak of the posterior distribution) and its 1σ uncertainty from the 68th percentile interval (HPDI; i.e., the narrowest interval containing 68%) of the posterior distribution. We conduct the spectral fitting for our sample of the 6 ($= 7 - 1$) galaxies (except GN-z11; see Section 2.3), one of which, Gz9p3, we exclude from our results. This is because we obtain only poor constraint on $[\text{Fe}/\text{H}]$ possibly due to the lack of S/N or the simple assumption of the constant and bursty star formation histories. Since the iron abundances of the other 5 ($= 6 - 1$) galaxies and GN-z11 are consistent within uncertainties for the constant and bursty star formation histories, we adopt the results based on the constant star formation history as the fiducial results. Figure 4 shows the examples of our fitting results of the high $[\text{Fe}/\text{H}]$ cases in the top and middle panels and low $[\text{Fe}/\text{H}]$ case in the bottom panel. We can see the differences of iron abundances in the observed spectra, comparing with the stellar model spectra. In Table 2, we present the best-fit parameters of the 6 galaxies in our sample. We obtain $[\text{Fe}/\text{H}]$ values for 4 galaxies and 3σ upper limits for 2 galaxies. As shown in Figure 6, we find that GS-z11-0 ($z=11.12$) have high $[\text{Fe}/\text{H}]$ as well as GN-z11 reported in Nakane et al. (2024).

3.1.2. AGN Iron Template Fitting

In Section 3.1.1, we derive the iron abundances, assuming that the UV continuum is dominated by stel-

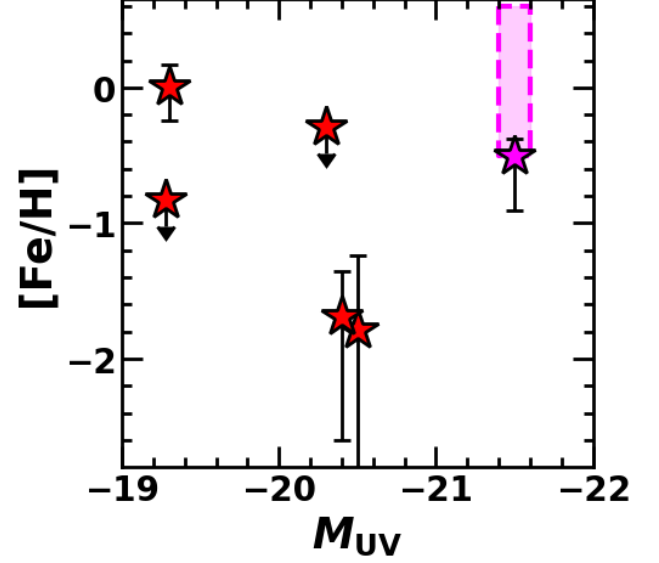


Figure 6. Fe/H ratio as a function of absolute UV magnitude. The magenta star symbol presents measurements of GN-z11 with the stellar models (Nakane et al. 2024). The red star symbols denote our measurements of the sample galaxies other than GN-z11. The magenta-shaded region represent our measurements of GN-z11 with the AGN models.

lar radiation. Out of the 2 galaxies, which have high $[\text{Fe}/\text{H}]$ values, GN-z11 have a possibility of hosting an AGN, as suggested based on the high ionization emission lines and signatures of high electron density (e.g., Maiolino et al. 2024). Actually, the Fe abundance of GN-z11 in the case where the UV continuum is dominated by AGN radiation is measured (Ji et al. 2024b). Ji et al. (2024b) investigate the continuum excess between $3000 - 3550 \text{ \AA}$ in the rest-frame wavelengths for the prism spectrum of GN-z11. Comparing the observed spectrum with the AGN models consisting of a power-law continuum, Balmer continuum, and Fe II complex at $3000 - 3550 \text{ \AA}$ calculated with CLOUDY, Ji et al. (2024b) obtain the lower limit of $[\text{Fe}/\text{H}] \gtrsim -0.5$. To further constrain $[\text{Fe}/\text{H}]$ of GN-z11 in the AGN case, we adopt an independent method, which compares the observed EWs of Fe II emission around $2200 - 3090 \text{ \AA}$ and Mg II $\lambda\lambda 2796, 2803$ lines with photoionization models, following Sameshima et al. (2017, 2020) and Onoue et al. (2020). We perform spectral fitting with the following AGN model,

$$F_\lambda^C = F_\lambda^{\text{PL}} + F_\lambda^{\text{BC}} + F_\lambda^{\text{FeII+FeIII}} + F_\lambda^{\text{MgII}}, \quad (1)$$

where $F_\lambda^{\text{PL}} = a\lambda^{-\beta}$, F_λ^{BC} , $F_\lambda^{\text{FeII+FeIII}}$, and F_λ^{MgII} represent the power-law continuum flux emitted from an accretion disk, Balmer continuum flux, iron pseudocontinuum flux, and Mg II $\lambda\lambda 2796, 2803$ line fluxes, respectively. For the Balmer continuum, we utilize the follow-

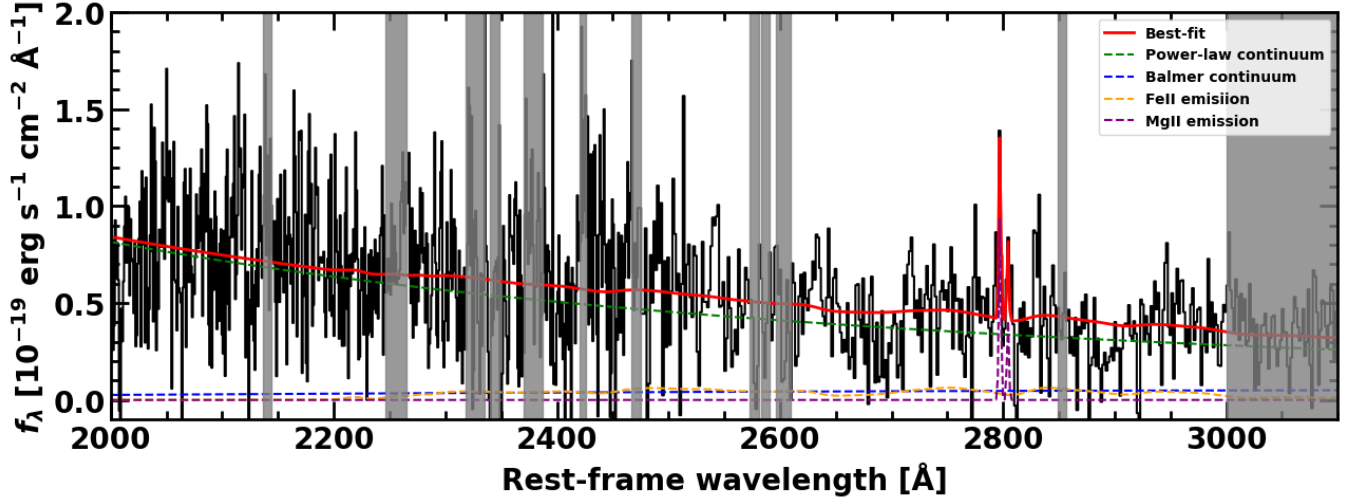


Figure 7. Results of the fitting for GN-z11 with the AGN models. The black and red solid lines present the observed grating spectrum and best-fit model spectrum, respectively. The green, blue, yellow, and purple dashed lines indicate the best-fit power-law continuum, Balmer continuum, Fe II emission, and Mg II emission, respectively. The gray-shaded regions denote the same as in Figure 4.

ing formula by Grandi (1982),

$$F_{\lambda}^{\text{BC}} = F_0^{\text{BE}} B_{\lambda}(T_e) \left[1 - e^{-\tau_{\text{BE}} \left(\frac{\lambda}{\lambda_{\text{BE}}} \right)^3} \right], \quad (2)$$

where F_0^{BE} , $B_{\lambda}(T_e)$, and τ_{BE} are the normalization factor, Planck function at electron temperature T_e , and optical depth at the Balmer edge $\lambda_{\text{BE}} = 3646 \text{ \AA}$. In this study, we adopt the fixed values of F_0^{BE} , T_e , and τ_{BE} , which are also used in the literature (Dietrich et al. 2003; Kurk et al. 2007; De Rosa et al. 2011; Mazzucchelli et al. 2017; Sameshima et al. 2017; Shin et al. 2019; Sameshima et al. 2020; Onoue et al. 2020). F_0^{BE} is fixed so that the Balmer continuum flux at $\lambda = 3675 \text{ \AA}$ is 30% of the power-law continuum flux at $\lambda = 3675 \text{ \AA}$. The other parameters of T_e and τ_{BE} are fixed to be $T_e = 15000 \text{ K}$ and $\tau_{\text{BE}} = 1$. For the iron pseudocontinuum, we use the Fe II template (Tsuzuki et al. 2006) broadened by convolution with a Gaussian function for which the FWHM is fixed at 800 km s^{-1} . Note that the FWHM of the convolved Gaussian function makes negligible effects on the measured Fe II flux, as pointed out in De Rosa et al. (2011). For the Mg II $\lambda\lambda 2796, 2803$ lines, we use double Gaussian functions, for which we fix the line widths and wavelength separation in the rest-frame of the two lines. There are seven free parameters in our AGN models (Equation 1), which are the amplitude a and slope β of the power-law continuum, normalization factor f of the iron pseudocontinuum, amplitudes a_1 and a_2 of the Mg II $\lambda 2796$ and Mg II $\lambda 2803$ lines, respectively, center wavelength λ_{cen} of Mg II $\lambda 2796$, and line width σ of Mg II $\lambda\lambda 2796, 2803$. We fit our AGN models to the grating spectrum of GN-z11 to exactly

measure the Mg II emissions. To obtain the PDFs of the parameters, we conduct MCMC simulations with `emcee` (Foreman-Mackey et al. 2013). Here, we check whether Fe II template is needed for the fitting based on the statistical indicator of Widely Applicable Information Criterion (WAIC; Watanabe 2010). WAIC is applicable to parameter estimation with posterior distributions unlike Akaike Information Criterion (AIC; Akaike 1973), which is used for maximum likelihood estimation. We calculate ΔWAIC , which is the difference between WAICs for the fitting with and without Fe II template. The obtained value is $\Delta\text{WAIC} = -41 < -10$, which means that including Fe II template enhances the goodness of the fitting. We determine the free parameter and 1σ uncertainty by the mode and 68th percentile HPDI of the posterior distribution, respectively. The best-fit parameters are $\log(a) = -10.45^{+0.23}_{-0.40}$, $\beta = -2.62^{+0.10}_{-0.10}$, $\log(f) = -6.09^{+0.21}_{-0.23}$, $\log(a_1) = -19.00^{+0.06}_{-0.14}$, $\lambda_{\text{cen}} = 2797.12^{+0.11}_{-0.41}$, $\sigma = 0.89^{+0.16}_{-0.35}$, and $\log(a_2) = -19.37^{+0.17}_{-0.23}$. In Figures 7 and 8, we present the best-fit AGN models and posterior PDFs of the parameters, respectively. We calculate the Fe II flux by integrating the best-fit Fe II template over the wavelength range of $2200 - 3090 \text{ \AA}$. We then derive the EW of Fe II, dividing the Fe II flux by the continuum flux at 3000 \AA . The EW of Mg II is obtained from the Mg II flux divided by the underneath continuum flux. To obtain Fe abundances, we compare the EWs of Fe II and Mg II with the models of Sameshima et al. (2020). Here, we need to correct the observed EWs for the Eddington ratio and continuum luminosity around 3000 \AA . This is because the EWs of Fe II and Mg II are correlated with Eddington ratio (e.g., Dong et al. 2011; Sameshima

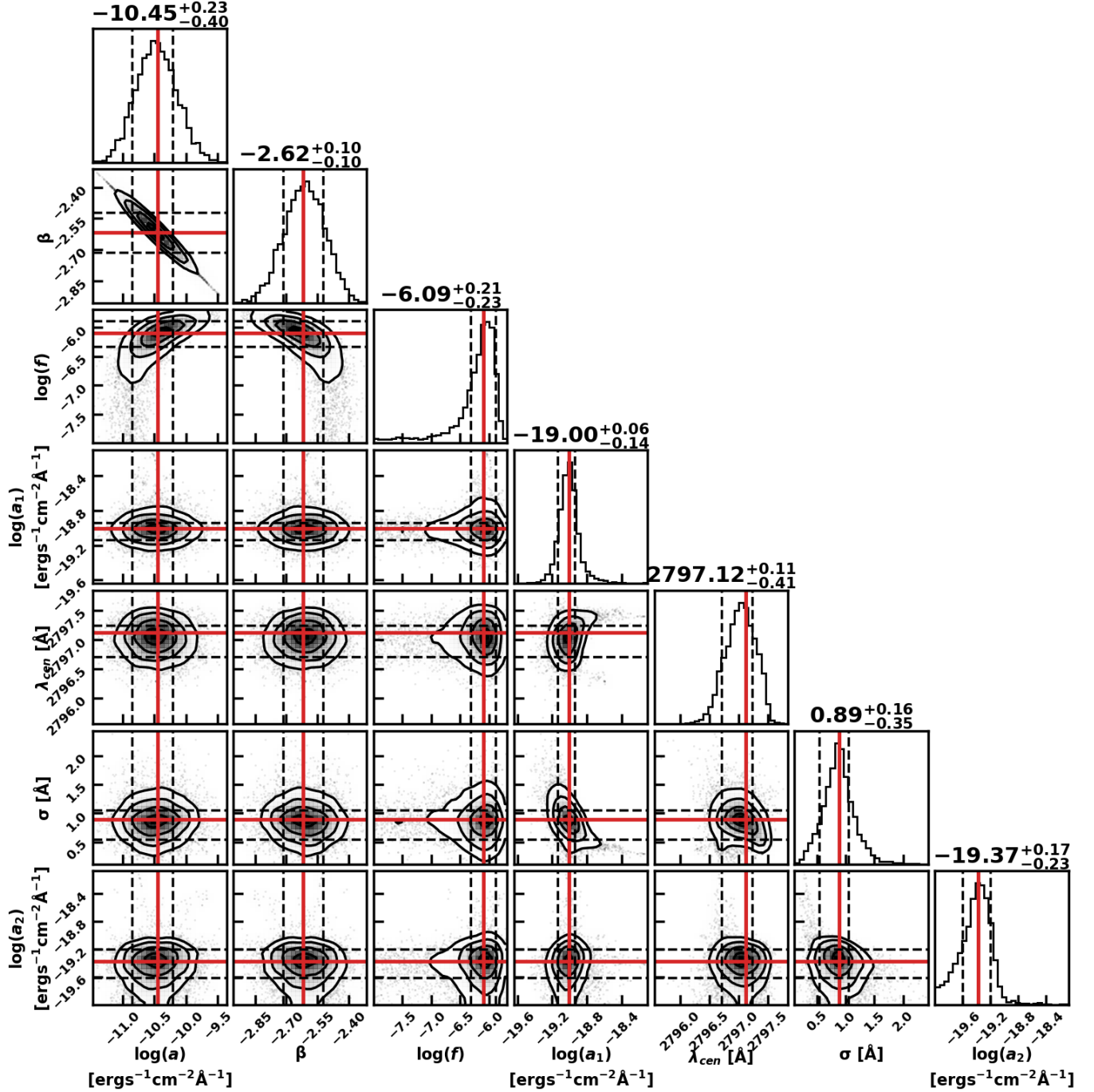


Figure 8. Posterior PDF of the fitting parameters obtained for the grating spectrum of GN-z11 with the AGN models. The symbols are the same as in Figure 5.

et al. 2017) and anticorrelated with continuum luminosity (Baldwin effect; e.g., Baldwin 1977; Baldwin et al. 1978), which may not be due to metallicity (e.g., Laor et al. 1995; Dietrich et al. 2002). We compare the corrected EWs of Fe II and Mg II derived from Equation (1) of Yoshii et al. (2022) with the abundance diagnostic diagram calculated with CLOUDY (Sameshima et al. 2020; Figure 9), and obtain $[\text{Fe}/\text{H}] \lesssim 0.6$. Combining with the

results of Ji et al. (2024b), we obtain the constraints of $-0.5 \lesssim [\text{Fe}/\text{H}] \lesssim 0.6$. In Figure 10, we present our $[\text{Fe}/\text{H}]$ measurement of GN-z11 with the AGN models, which is comparable to those with the stellar models.

3.2. Oxygen Abundance Measurement

To measure oxygen abundances, we measure emission line fluxes by performing spectral fitting with the lin-

Table 1. Sample in This Study

Name	z_{spec}	M_{UV} (mag)	$\log M_*$ (M_{\odot})	Ref.
(1)	(2)	(3)	(4)	(5)
Gz9p3	9.313	−21.6	$9.2^{+0.1}_{-0.2}$	Bo23
GS-z9-0	9.433	−20.4	$8.18^{+0.06}_{-0.06}$	Bu24, Cu24, Jo24
JADES6438	9.689	−19.28	-	Bu24, Jo24
MACS0647-JD	10.17	−20.3	7.6 ± 0.1	Hs24
GN-z11	10.603	−21.5	$9.1^{+0.4}_{-0.3}$	Bu23, Ta23
GS-z11-0	11.122	−19.3	$8.3^{+0.1}_{-0.1}$	Ha24
GHZ2	12.34	−20.5	$9.05^{+0.10}_{-0.25}$	Ca24

(1) Name. (2) Spectroscopic redshift. (3) Absolute UV magnitude. (4) Stellar mass. (5) References for spectroscopic redshift, absolute UV magnitude, and stellar mass (Bo23: [Boyett et al. 2023](#), Bu23: [Bunker et al. 2023](#), Ta23: [Tacchella et al. 2023](#), Bu24: [Bunker et al. 2024](#), Ca24: [Castellano et al. 2024](#), Cu24: [Curti et al. 2024](#), Jo24: [Jones et al. 2024](#) Ha24: [Hainline et al. 2024](#), Hs24: [Hsiao et al. 2024](#)).

Table 2. Best-fit Parameters for Fitting with the Stellar Models

Name	z_{spec}	[Fe/H]	$\log(t/\text{yr})$	E(B-V)	$\log(f)$
(1)	(2)	(3)	(4)	(5)	(6)
GHZ2	12.34	$-1.78^{+0.54}_{-1.31}$	$6.13^{+1.01}_{-0.08}$	$0.01^{+0.02}_{-0.01}$	$-0.16^{+0.04}_{-0.08}$
GS-z11-0	11.122	$0.00^{+0.16}_{-0.25}$	$7.96^{+0.17}_{-0.85}$	$0.00^{+0.04}_{-0.00}$	$-0.03^{+0.16}_{-0.01}$
GN-z11 [†]	10.603	$-0.50^{+0.12}_{-0.40}$	$7.41^{+0.79}_{-0.42}$	$0.07^{+0.02}_{-0.04}$	$0.21^{+0.05}_{-0.17}$
MACS0647-JD	10.17	< -0.29	$7.93^{+0.17}_{-0.66}$	$0.02^{+0.01}_{-0.02}$	$-0.01^{+0.06}_{-0.03}$
JADES6438	9.689	< -0.83	$7.48^{+0.63}_{-0.80}$	$0.06^{+0.01}_{-0.03}$	$0.14^{+0.04}_{-0.13}$
GS-z9-0	9.433	$-1.69^{+0.33}_{-0.92}$	$6.08^{+0.20}_{-0.05}$	$0.00^{+0.00}_{-0.00}$	$-0.15^{+0.03}_{-0.02}$

(1) Name. (2) Spectroscopic redshift. (3) Iron abundance and the 3σ upper limit. (4) Stellar age. (5) Color excess. (6) Normalization factor.

[†] The measurements are from [Nakane et al. \(2024\)](#) based on the medium-resolution grating spectra.

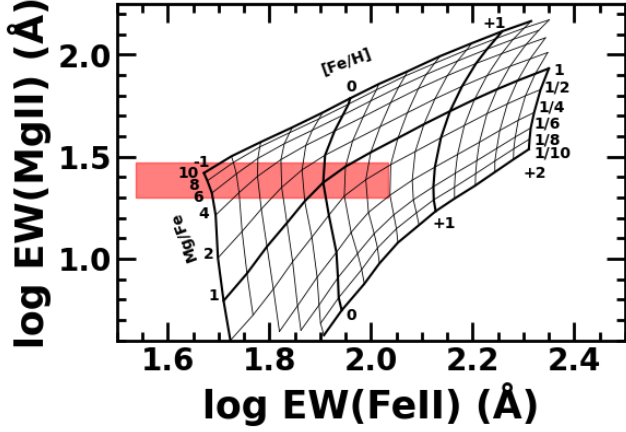


Figure 9. Abundance diagnostic diagram. The grid lines show the calculated $\text{EW}(\text{Mg II})$ and $\text{EW}(\text{Fe II})$ as functions of Mg/Fe ($= 10^{[\text{Mg}/\text{Fe}]}$) and $[\text{Fe}/\text{H}]$ (Sameshima et al. 2020). The red-shaded region denotes the measurements of GN-z11 with the AGN models.

ear combination of a Gaussian function and a constant value, $A \exp[-(\lambda - \lambda_{\text{cen}})^2 / 2\sigma^2] + F_{\text{cont}}$, where A , λ_{cen} , σ , and F_{cont} are the line amplitude, center wavelength, dispersion, and continuum flux, respectively. To obtain the PDFs of the parameters, we perform MCMC simulations with *emcee* (Foreman-Mackey et al. 2013). We obtain the line flux (1σ uncertainty) from the mode (68th percentile HPDI) of the probability distribution calculated with the posterior distributions of the free parameters.

For the galaxies with the $[\text{O III}] \lambda 4363$ lines detected, the O/H values are measured with the direct- T_e method: GN-z11 (stellar case; Cameron et al. 2023, AGN case; Álvarez-Márquez et al. 2024), MACS0647-JD (Hsiao et al. 2024), and GS-z9-0 (Curti et al. 2024). For the other 3 galaxies with no detection of $[\text{O III}] \lambda 4363$ lines, the O/H values are measured with the strong line method: GHZ2 (Castellano et al. 2024), GS-z11-0, and JADES6438 (this work). The strong line methods are based on the empirical relations between line ratios of strong emissions and oxygen abundances derived with the direct- T_e method (e.g., Nakajima et al. 2022; Curti et al. 2023; Sanders et al. 2024). Hereafter, we refer to the lines ratios of $[\text{O II}] \lambda \lambda 3726, 3729 / \text{H}\beta$ and $[\text{Ne III}] \lambda 3869 / [\text{O II}] \lambda \lambda 3726, 3729$ as R2 and Ne3O2, respectively. We use the oxygen abundance of GHZ2 (Castellano et al. 2024), $12 + \log(\text{O}/\text{H}) = 7.26^{+0.27}_{-0.24}$, measured from the relation between Ne3O2 and $12 + \log(\text{O}/\text{H})$ (Curti et al. 2023). We estimate the oxygen abundances and their errors of JADES6438 and GS-z11-0 by conducting Monte Carlo simulations. We derive 1000 values of $12 + \log(\text{O}/\text{H})$ by fluctuating the observed fluxes and R2 (Ne3O2) versus O/H relation with their 1σ un-

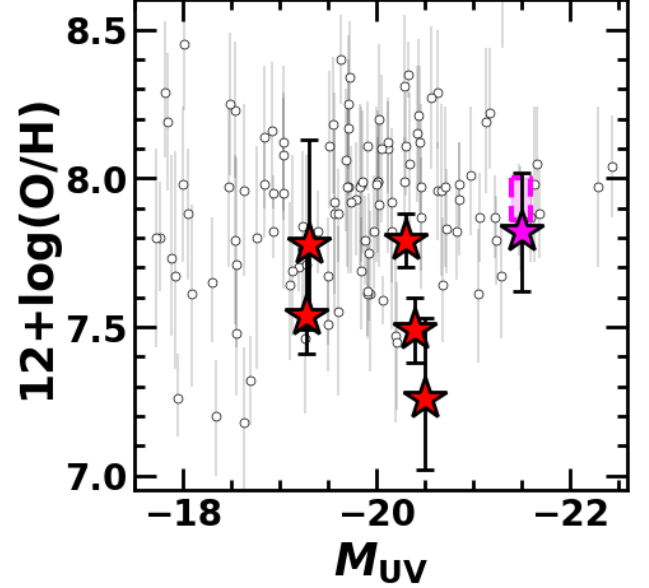


Figure 10. O/H ratio as a function of absolute UV magnitude. The star symbols show the measurements of the 6 galaxies in our sample (this work, Cameron et al. 2023; Castellano et al. 2024; Hsiao et al. 2024). The open circles indicate the measurements of galaxies at $z \sim 4-9$ (Nakajima et al. 2023).

certainties assuming the normal distribution. We then determine the $12 + \log(\text{O}/\text{H})$ values and 1σ errors from the median and 16th/84th percentiles of the distribution for the 1000 values of $12 + \log(\text{O}/\text{H})$, respectively. For JADES6438, we measure O/H from the observed value of $\text{R2} = 0.39^{+0.16}_{-0.14}$ and relation in Curti et al. (2017, 2020), and obtain $12 + \log(\text{O}/\text{H}) = 7.54^{+0.22}_{-0.13}$. We obtain $12 + \log(\text{O}/\text{H}) = 7.78^{+0.35}_{-0.29}$ for GS-z11-0 from the observed value of $\text{Ne3O2} = 0.72^{+0.41}_{-0.41}$ with the relation in Curti et al. (2023). Although the Ne3O2 versus O/H relation is scattered compared to the other line ratios (e.g., Figure 4 in Nakajima et al. 2022), the effects of different calibrations for the Ne3O2 versus O/H relation on the O/H measurements are within the uncertainties (see also Figure 5 in Curti et al. 2023), which does not change our results. In Table 3 and Figure 10, we show the oxygen abundance measurements for our sample in this work and the literature, which are comparable to those of $z \sim 4-9$ galaxies (Nakajima et al. 2023).

3.3. Abundance Ratios of $[\text{O}/\text{Fe}]$

To derive O/Fe, we combine Fe/H and O/H measurements. Here, note that chemical abundances of massive stars (i.e., Fe/H) should be similar to those of the surrounding ionized gas (i.e., O/H) because their lifetimes are short (Steidel et al. 2016; Cullen et al. 2019; Harikane et al. 2020; Cullen et al. 2021; Kashino et al.

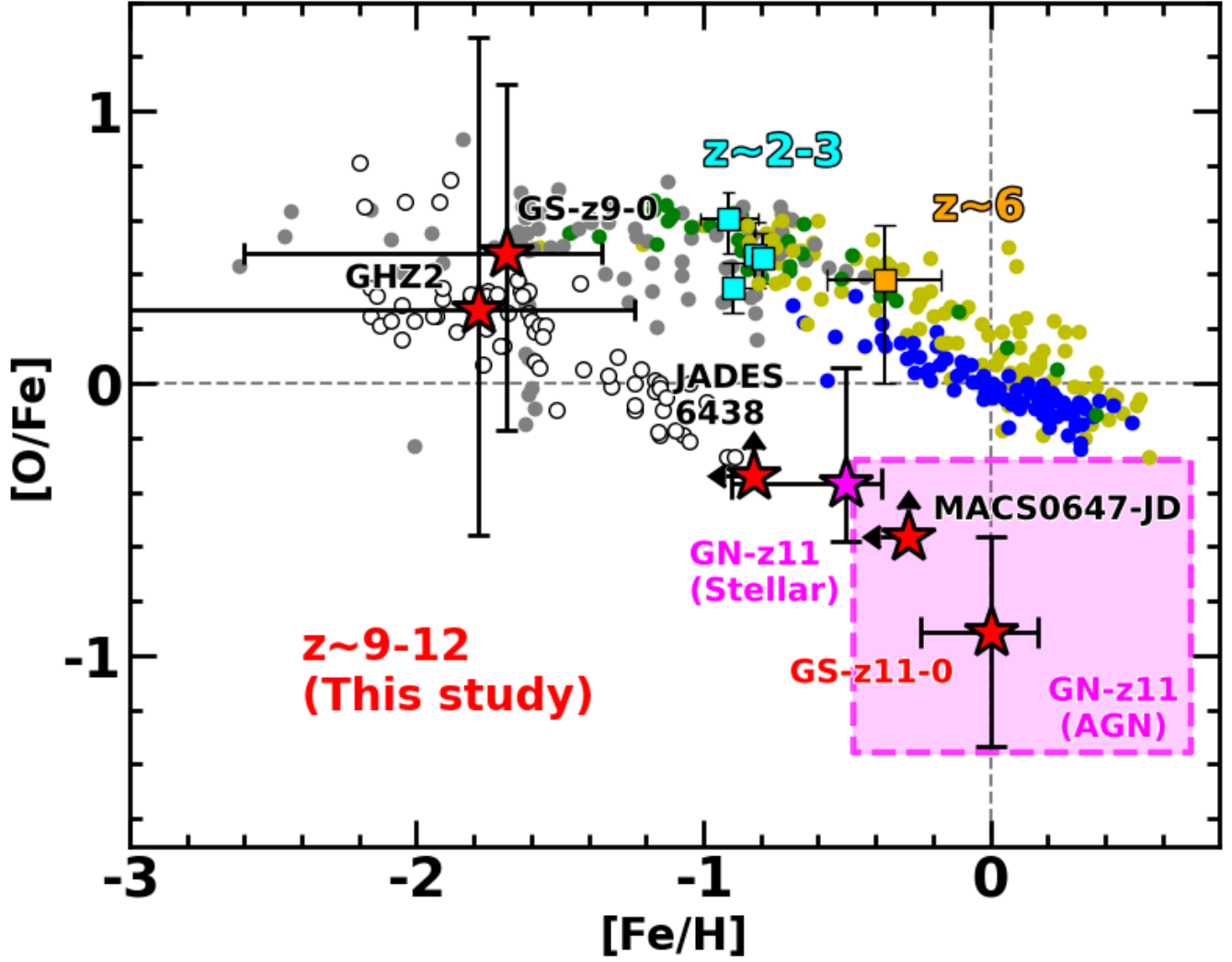


Figure 11. O/Fe as a function of Fe/H . The star symbols and magenta shaded region show the same as in Figure 6. The cyan and orange squares show the measurements for the composite spectra of star-forming galaxies at $z \sim 2-3$ (Steidel et al. 2016; Cullen et al. 2021; Kashino et al. 2022) and 6 (Harikane et al. 2020). The yellow, green, blue, and gray circles denote the measurements for the MW stars (Meléndez et al. 2003; Carretta et al. 2005; Yong et al. 2005; Lecureur et al. 2007; Pasquini et al. 2008; Yong et al. 2008; Carretta et al. 2010; Valenti et al. 2011; Bensby et al. 2013; Zhao et al. 2016; Amarsi et al. 2019) in the bulge, thick disk, thin disk, and halo, respectively. The white circles indicate the measurements of the metal-poor stars in the Sculptor galaxy (Hill et al. 2019; Tang et al. 2023). The gray-dashed lines denote the solar abundance ratios.

2022; Nakane et al. 2024). We thus adopt the ratio of the gas-phase O/H to the stellar Fe/H as a proxy of the instantaneous O/Fe in the galaxy. We derive $[O/Fe]$ ratios with $[O/Fe] = [O/H] - [Fe/H]$ for our sample. We summarize the chemical abundance measurements of our sample in Table 3. In Figures 11 and 12, we compare our $[O/Fe]$ measurements with those of MW stars (Meléndez et al. 2003; Carretta et al. 2005; Yong et al. 2005; Lecureur et al. 2007; Pasquini et al. 2008; Yong et al. 2008; Carretta et al. 2010; Valenti et al. 2011; Bensby et al. 2013; Zhao et al. 2016; Amarsi et al. 2019), metal-poor stars in Sculptor galaxy (Hill et al. 2019; Tang et al. 2023) and composite spectra of star-

forming galaxies at $z \sim 2-3$ (Steidel et al. 2016; Cullen et al. 2021; Kashino et al. 2022) and 6 (Harikane et al. 2020). We find that majority of (4 out of 6) galaxies are consistent with iron-poor abundance ratios ($[O/Fe] \gtrsim 0$) like the halo stars in the MW and metal-poor stars in the Sculptor galaxy. This high $[O/Fe]$ ratios of the 4 galaxies at $z \sim 9-12$ are explained by the chemical enrichment of CCSNe as well as the galaxies at $z \sim 2-6$ (Steidel et al. 2016; Cullen et al. 2019; Harikane et al. 2020; Cullen et al. 2021; Kashino et al. 2022). In contrast, 2 out of 6 galaxies, GS-z11-0 and GN-z11, show Fe enhancements ($[O/Fe] < 0$) compared to the MW stars and low-redshift galaxies at the same $[Fe/H]$ and

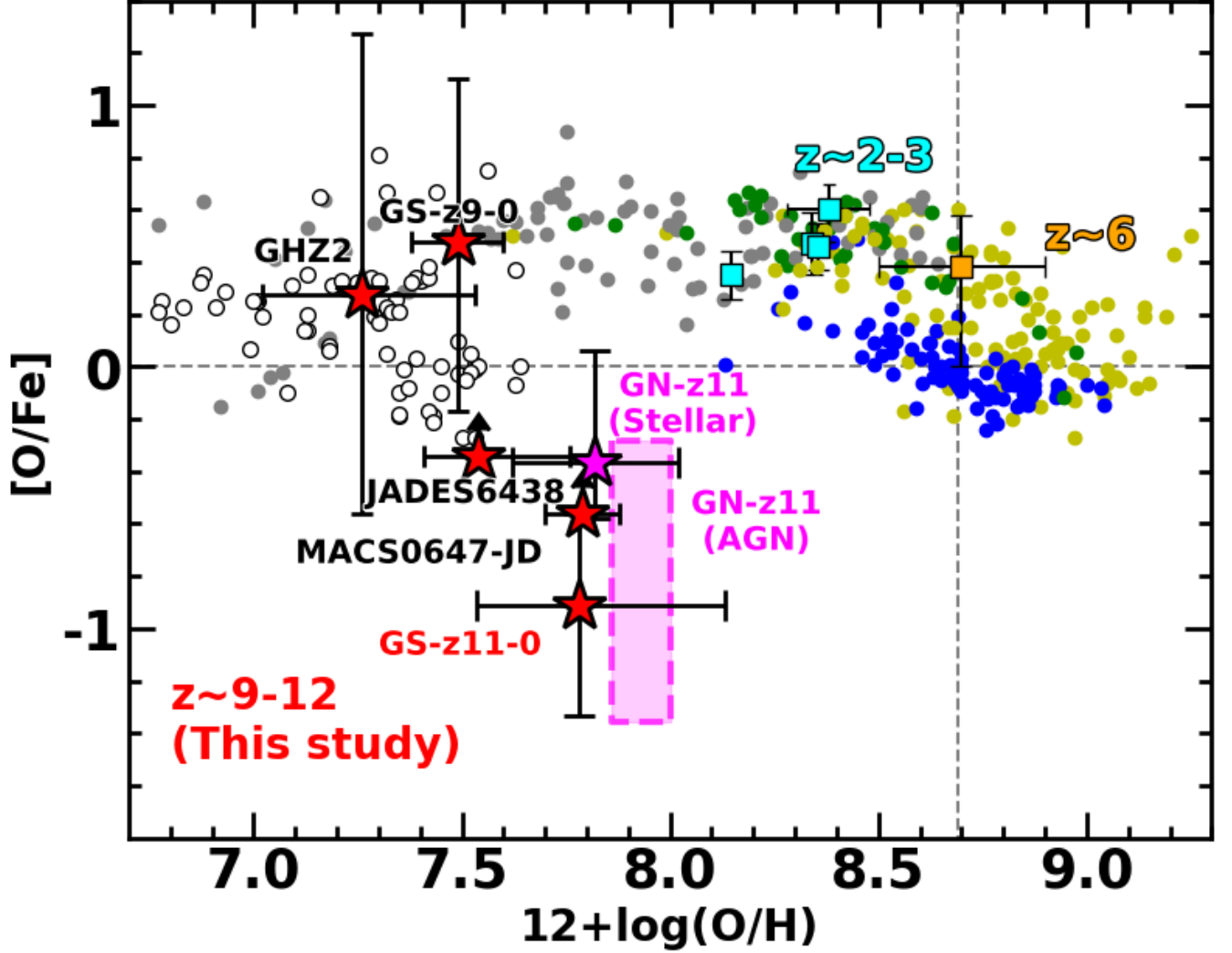


Figure 12. O/Fe as a function of O/H . The symbols are the same as in Figure 11.

$12+\log(O/H)$ values. We note that GN-z11 may be a Fe-enhanced population regardless of the origin of UV emission dominated by stars or AGNs. The Fe enhancements of GS-11-0 and GN-z11 cannot be explained only by the chemical enrichment of CCSNe.

4. DISCUSSION

4.1. Fe Enhancement by Supernovae

As described in Section 3.3, we find the low $[O/Fe]$ ratios of GN-z11 and GS-z11-0 compared to the MW stars and low-redshift galaxies (Figures 11 and 12). To explore the origins of such low $[O/Fe]$, we compare $[O/Fe]$ measurements with the supernova yield models of CCSNe, HNe, BrHNe, PISNe, and SNeIa. We use the CCSN and HN yields of Nomoto et al. (2013) with the progenitor mass of $20 - 40 M_{\odot}$ and the metallicity of $Z_{*} = 0.004$, which is comparable to our measurements. The CCSN and HN yield models have different

explosion energies E . While the explosion energies are $E_{51} = E/10^{51} \text{ erg} = 1$ for all of the CCSN yield models, those of the HN yield models are larger values of $E_{51} = 10, 10, 20$, and 30 for the progenitor mass of $20, 25, 30$, and $40 M_{\odot}$, respectively. The amount of Fe ejected by the supernovae also depends on the mass cut that divides the ejecta and compact remnant as well as the explosion energy. The mass cuts of HN yield models are set to explain the yield of the observed HNe (e.g., Nomoto et al. 2004). We utilize the BrHN yields of Umeda & Nomoto (2008) with the highest explosion energy of $E_{51} = 50, 150, 100, 110$, and 210 for the progenitor mass of $30, 50, 80, 90$ and $100 M_{\odot}$, respectively, and lowest mass cut just above the Fe core for a certain progenitor mass within $30 - 100 M_{\odot}$ (see Table 3 in Umeda & Nomoto 2008). The O/Fe ratios of BrHNe are thus the lowest among the HNe at the same progenitor mass. We take the nonrotating PISNe yields of Taka-

Table 3. Abundance Ratio Measurements

Name (1)	z_{spec} (2)	[Fe/H] (3)	$12 + \log(\text{O}/\text{H})$ (4)	[O/Fe] (5)	Ref. (6)
GHZ2	12.34	$-1.78^{+0.54}_{-1.31}$	$7.26^{+0.27}_{-0.24}$	$0.27^{+1.00}_{-0.83}$	Castellano et al. (2024)
GS-z11-0	11.122	$0.00^{+0.16}_{-0.25}$	$7.78^{+0.35}_{-0.29}$	$-0.91^{+0.35}_{-0.42}$	This work
GN-z11 (Stellar)	10.6034	$-0.50^{+0.12}_{-0.40}$	7.82 ± 0.20	$-0.37^{+0.43}_{-0.22}$	Cameron et al. (2023)
GN-z11 (AGN)	10.6034	$-0.5-0.6$	$7.93 \pm 0.07^{\dagger}$	$-1.4- -0.3$	Álvarez-Márquez et al. (2024)
MACS0647-JD	10.17	< -0.29	7.79 ± 0.09	> -0.56	Hsiao et al. (2024)
JADES6438	9.689	< -0.83	$7.54^{+0.22}_{-0.13}$	> -0.34	This work
GS-z9-0	9.433	$-1.69^{+0.33}_{-0.92}$	7.49 ± 0.11	$0.10^{+0.85}_{-0.37}$	Curti et al. (2024)

(1) Name. (2) Spectroscopic redshift. (3) Iron abundance and the 3σ upper limit. (4) Oxygen abundance. (5) O/Fe abundance ratio the 3σ lower limit. (6) References for oxygen abundances.

\dagger The uncertainty of $12+\log(\text{O}/\text{H})$ measurement based on the stellar radiation (Álvarez-Márquez et al. 2024) is adopted.

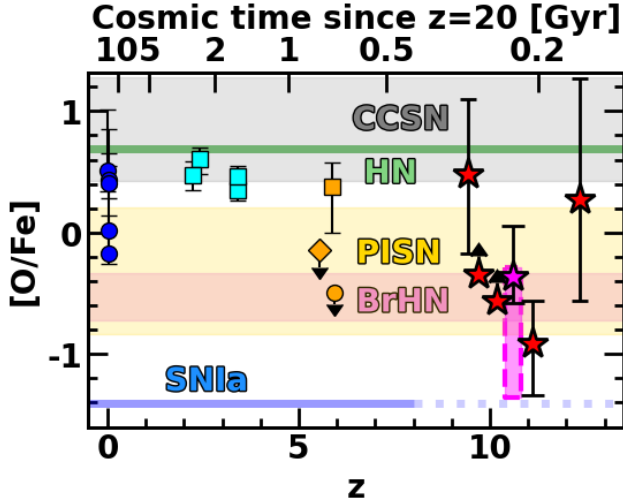


Figure 13. Redshift evolution of [O/Fe]. The cyan, orange, red and magenta symbols are the same as in Figure 12. The orange circles indicate the measurements for $z \sim 6$ galaxies of GS-3073 (Ji et al. 2024a) and GS9422 (Tacchella et al. 2024). The blue circles denote the measurements for local EMPGs (Izotov et al. 2018; Kojima et al. 2020; Isobe et al. 2022). The gray, green, pink, and yellow shaded regions represent the yield models of CCSNe, HNe, BrHNe, and PISNe, respectively.

hashi et al. (2018) with the progenitor mass of $220 - 280 M_{\odot}$. For SN Ia yields, we use the models with delayed detonation of Chandrasekhar mass C+O white dwarf in a single degenerate system (W7 model; Nomoto et al. 1984), whose data are taken from Iwamoto et al. (1999).

In Figure 13, we present a redshift evolution of [O/Fe] for galaxies with the yield models and cosmic age since $z = 20$ (~ 200 Myr after the Big Bang), when the first star formation is expected to occur based on the

standard Λ -CDM scenario (e.g., Tegmark et al. 1997). The iron-poor abundance ratios of the 4 galaxies are explained by the standard CCSNe as well as the $z \sim 2 - 6$ galaxies (Steidel et al. 2016; Cullen et al. 2019; Harikane et al. 2020; Cullen et al. 2021) while the iron enhancement of GS-z11-0 and GN-z11 require BrHNe, PISNe, or SNe Ia. Here, the timescale of these supernovae is important. While BrHNe and PISNe instantaneously occur after the formation of massive stars (\sim a few Myr; e.g., Nomoto et al. 2013), SNe Ia need the delay time (typically \sim a few hundreds of Myr; e.g., Chen et al. 2021) for white dwarf formation and gas accretion/white dwarf merger. The short timescale of BrHNe/PISNe makes it difficult to observe low [O/Fe] ratios for $\sim 30\%$ ($= 2/6$) of the galaxies during $z = 9.3 - 12.3$ (~ 150 Myr). Conversely, based on the long timescale due to the delay time, SNe Ia may have difficulty in causing Fe enhancement at as early as $z \sim 10$, when the age of the universe is only ~ 450 Myr. In the following sections, we examine which SNe mainly contribute to the observed low [O/Fe] ratios with the chemical evolution models.

4.2. Chemical Evolution Models

To evaluate the Fe enhancement by PISNe or SNe Ia, we construct PISN and SN Ia models with reference to Suzuki & Maeda (2018). Although we do not construct BrHN models, we discuss the possibility of Fe enhancements by BrHNe in Section 4.3. We define the [O/Fe] ratio at each age in the PISN (SN Ia) model as the ratio of the total numbers of oxygen and iron ejected by CCSNe and PISNe (SNe Ia) which have already occurred before the age. We present an overview for the processes of the model construction in Figure 14. In the PISN and SN Ia models, stars instantaneously formed

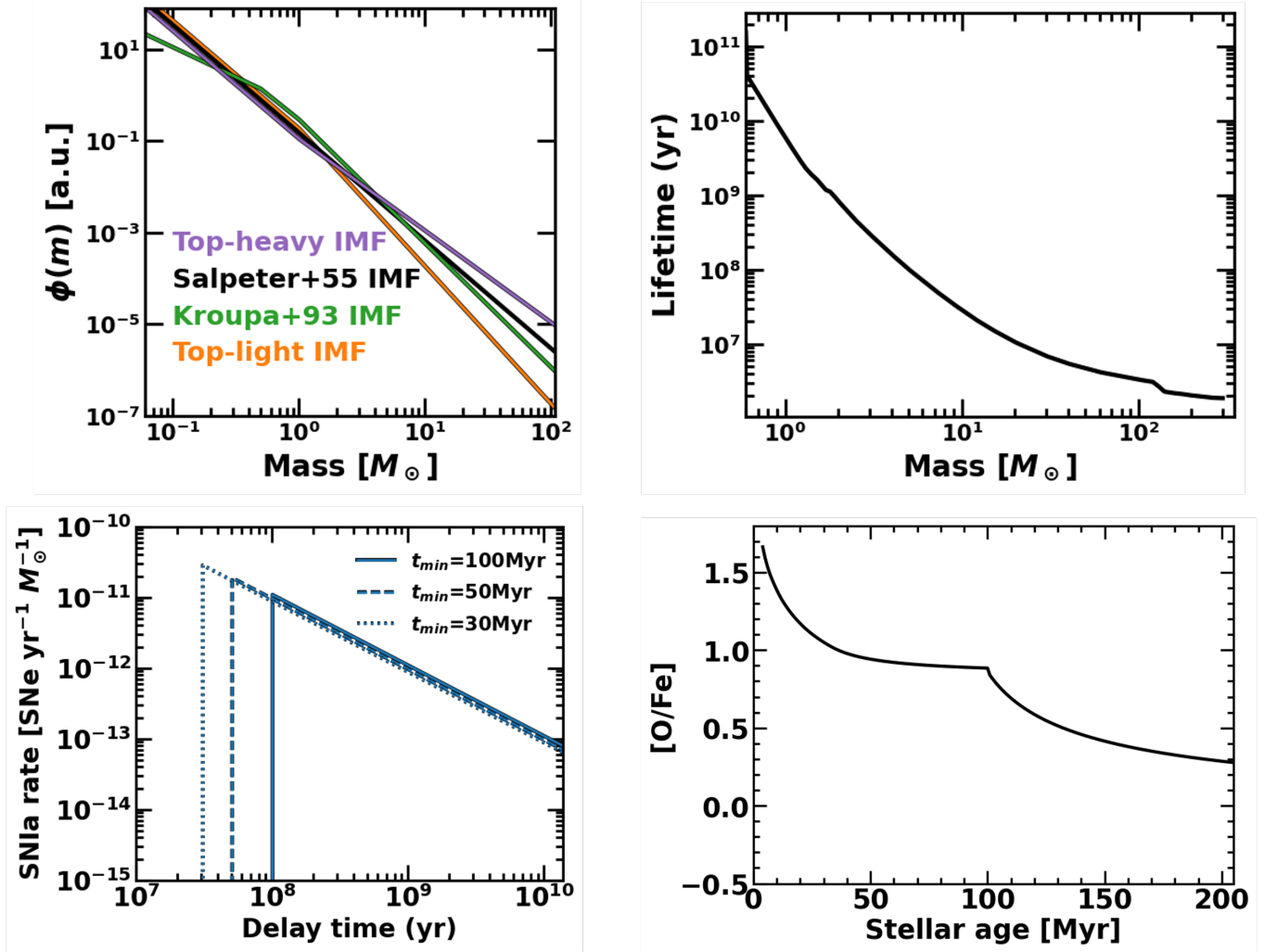


Figure 14. An overview of the construction processes for the PISN and SN Ia models. Top left: Initial mass function. The purple, black, green, and orange lines show the top-heavy, Salpeter (1955), Kroupa et al. (1993), and top-light IMF, respectively. Top right: Stellar lifetime as a function of stellar mass. The black line is derived with stellar evolution models (Padovani & Matteucci 1993; Takahashi et al. 2018). Bottom left: Delay time distribution for SNe Ia. The solid, dashed, and dotted line correspond to the minimum delay time of $t_{\min} = 100, 50$, and 30 Myr, respectively. Bottom right: $[\text{O}/\text{Fe}]$ ratio as a function of stellar age. The black line represents an example of the SN Ia model with the delay time of $t_{\min} = 100$ Myr.

based on the IMF. We use the IMF given by Salpeter (1955), which is expressed by the power-law function of $\xi(M) = dN/dM \propto M^{-\alpha}$ with $\alpha = 2.35$ for entire mass ranges. We normalize the IMF to be the numbers of stars with mass $[M, M + dM]$ per $1M_{\odot}$ of star formation. The distribution $\Phi(M)$ is given by

$$\Phi(M) = C\xi(M)$$

$$C^{-1} = \int_{M_{\min}}^{M_{\max}} M\xi(M)dM, \quad (3)$$

where M_{\min} and M_{\max} are the lower and upper limits for the masses of stars, respectively. We use the fixed values of $M_{\min} = 0.08M_{\odot}$ and $M_{\max} = 300M_{\odot}$ ($100M_{\odot}$) for the PISN (SN Ia) model. For comparison, we also use

the IMF given by Kroupa et al. (1993),

$$\alpha = \begin{cases} 2.35 & \text{for } M < 2M_{\odot}, \\ 2.7 & \text{for } M \geq 2M_{\odot}, \end{cases} \quad (4)$$

top-heavy IMF,

$$\alpha = \begin{cases} 2.35 & \text{for } M < 2M_{\odot}, \\ 2.0 & \text{for } M \geq 2M_{\odot}, \end{cases} \quad (5)$$

and top-light IMF,

$$\alpha = \begin{cases} 2.35 & \text{for } M < 2M_{\odot}, \\ 3.0 & \text{for } M \geq 2M_{\odot}. \end{cases} \quad (6)$$

In both the PISN and SN Ia models, the stars with masses of $9M_{\odot} < M < 100M_{\odot}$ cause CCSNe at the end of their lifetimes expressed by the following formula from Padovani & Matteucci (1993),

$$\tau(M) = \begin{cases} 160 & \text{Gyr } (M < 0.6M_{\odot}), \\ 10^{(0.334-q(M)^{0.5})/0.116} & \text{Gyr } (0.6 \leq M \leq 6.0M_{\odot}), \\ 1.2M^{-1.85} + 0.003 & \text{Gyr } (M \geq 6.0M_{\odot}), \end{cases} \quad (7)$$

with

$$q(M) = 1.790 - 0.2232[7.764 - \log_{10}(M)]. \quad (8)$$

We derive the IMF-averaged mass ejecta for an element i produced by CCSNe with

$$M_i^{\text{CC}} = \int_0^t dt' \int_{9M_{\odot}}^{100M_{\odot}} dM Y_i^{\text{CC}}(M) \Phi(M) \text{SFR}(t' - \tau(M)), \quad (9)$$

where Y_i^{CC} , t , and $\text{SFR}(t)$ are the yield mass of the element i produced by CCSN, stellar age, and star formation rate at t , respectively. We use the models with the metallicity $Z = 0.004$ provided by Nomoto et al. (2013) for Y_i^{CC} . We assume a constant star formation history to calculate $\text{SFR}(t)$ for our fiducial models, which is aligned with that our fiducial measurements of $[\text{O}/\text{Fe}]$ are based on the constant star formation history. To investigate the effects of the star formation history, we also adopt the decreasing and increasing star formation histories, obtained with the SED fitting for GS-11-0 (Hainline et al. 2024) and GN-z11 (Tacchella et al. 2023). In the PISN models, we also calculate the IMF-averaged yields of PISNe, which is caused by the stars with the masses of $140M_{\odot} < M < 300M_{\odot}$ at the end of their lifetimes (Takahashi et al. 2018), in the same way as CCSNe. We consider two types of yields for the PISN models, CCSNe + PISNe with and without failed supernovae, which directly collapse into black holes and do not eject any gas (e.g., Ebinger et al. 2020). We assume no ejecta for the stars with masses of $25M_{\odot} < M < 140M_{\odot}$ if we add failed supernovae. For SNe Ia, we consider delay time distribution (DTD), which is the probability distribution of the number of SNe Ia occurring with a delay time. We use the DTD with a power-law function form of $\propto t^{-1}$ (e.g., Rodney et al. 2014),

$$\text{DTD}(t) = \frac{N_{\text{Ia}} t^{-1}}{\ln(t_{\text{max}}/t_{\text{min}})} \Theta(t - t_{\text{min}}), \quad (10)$$

where N_{Ia} , t_{min} , t_{max} , and $\Theta(x)$ indicate the SN Ia rate, minimum delay time, cosmic age at present ($= 13.8 \text{ Gyr}$), and Heaviside step function, respectively. The SN Ia rate, the time-integrated number of SNe Ia

per $1M_{\odot}$, is measured to be $\sim (1-7) \times 10^{-3} M_{\odot}^{-1}$ (e.g., Rodney et al. 2014; Maoz & Graur 2017) and fixed to be $N_{\text{Ia}} = 5.4 \times 10^{-3} M_{\odot}^{-1}$ (Maoz & Graur 2017) in our SN Ia models. We set three types of the minimum delay time of $t_{\text{min}} = 30 \text{ Myr}$, 50 Myr , and 100 Myr (e.g., Totani et al. 2008; Maoz et al. 2014; Rodney et al. 2014; Maiolino & Mannucci 2019). We calculate the mass for an element i ejected by SNe Ia with the delay time distribution, described as

$$M_i^{\text{Ia}} = \int_{t_{\text{min}}}^t d\tau \int_{t_{\text{min}}}^{\tau} dt' Y_i^{\text{Ia}} \text{DTD}(t') \text{SFR}(\tau - t'), \quad (11)$$

where Y_i^{Ia} is the yield mass of the element i produced by SN Ia. We use the W7 model (Nomoto et al. 1984; Iwamoto et al. 1999; see Section 4.1) for Y_i^{Ia} . We derive $[\text{O}/\text{Fe}]$ ratios as a function of t for the PISN (SN Ia) models by converting the ratios of the mass ejected by CCSNe and PISNe (SNe Ia) to the number ratios.

4.3. Origins of Low $[\text{O}/\text{Fe}]$ Ratios

In Figures 15 and 16, we compare the $[\text{O}/\text{Fe}]$ values of GS-z11-0/GN-z11 with the PISN and SN Ia models, respectively. We take the values of stellar age measured from the SED fitting in the literature ($t = 158_{-32}^{+42} \text{ Myr}$ for GS-z11-0; Hainline et al. 2024 and $t = 24_{-10}^{+20} \text{ Myr}$ for GN-z11; Tacchella et al. 2023). Note that for GN-z11, we adopt the value measured from the combined photometry of the point source and extended component. The point source and extended component have stellar ages of $t = 11_{-7}^{+58} \text{ Myr}$ and $t = 35_{-19}^{+15} \text{ Myr}$, respectively. The top panels present our fiducial models with the assumption of the constant star formation history. While the PISN models cannot explain the low $[\text{O}/\text{Fe}]$ values regardless of the IMF slope and existence of failed SNe, the yields of only PISN (yellow shaded region in Figure 15) can explain the low $[\text{O}/\text{Fe}]$ values. In this case, BrHNe may also be the cause of Fe enhancement (see Figure 13). In the SN Ia case, the SN Ia models cannot explain the low $[\text{O}/\text{Fe}]$ values except for the models with the short delay time ($t_{\text{min}} \sim 30-50 \text{ Myr}$) and top-light IMF. We also develop the PISN and SN Ia models under the assumption of the decreasing and increasing star formation histories, as shown in the middle and bottom panels, respectively. The decreasing star formation history has negligible effects on both the PISN and SNIa models. While the increasing star formation history does not largely change the PISN models, it elevates the $[\text{O}/\text{Fe}]$ ratios of the SN Ia models, which makes it somewhat difficult to explain low $[\text{O}/\text{Fe}]$ ratios of GN-z11. We note that the increasing star formation history is obtained for the point source in GN-z11. If the Fe enhancement of GN-z11 occurs in the point source region,

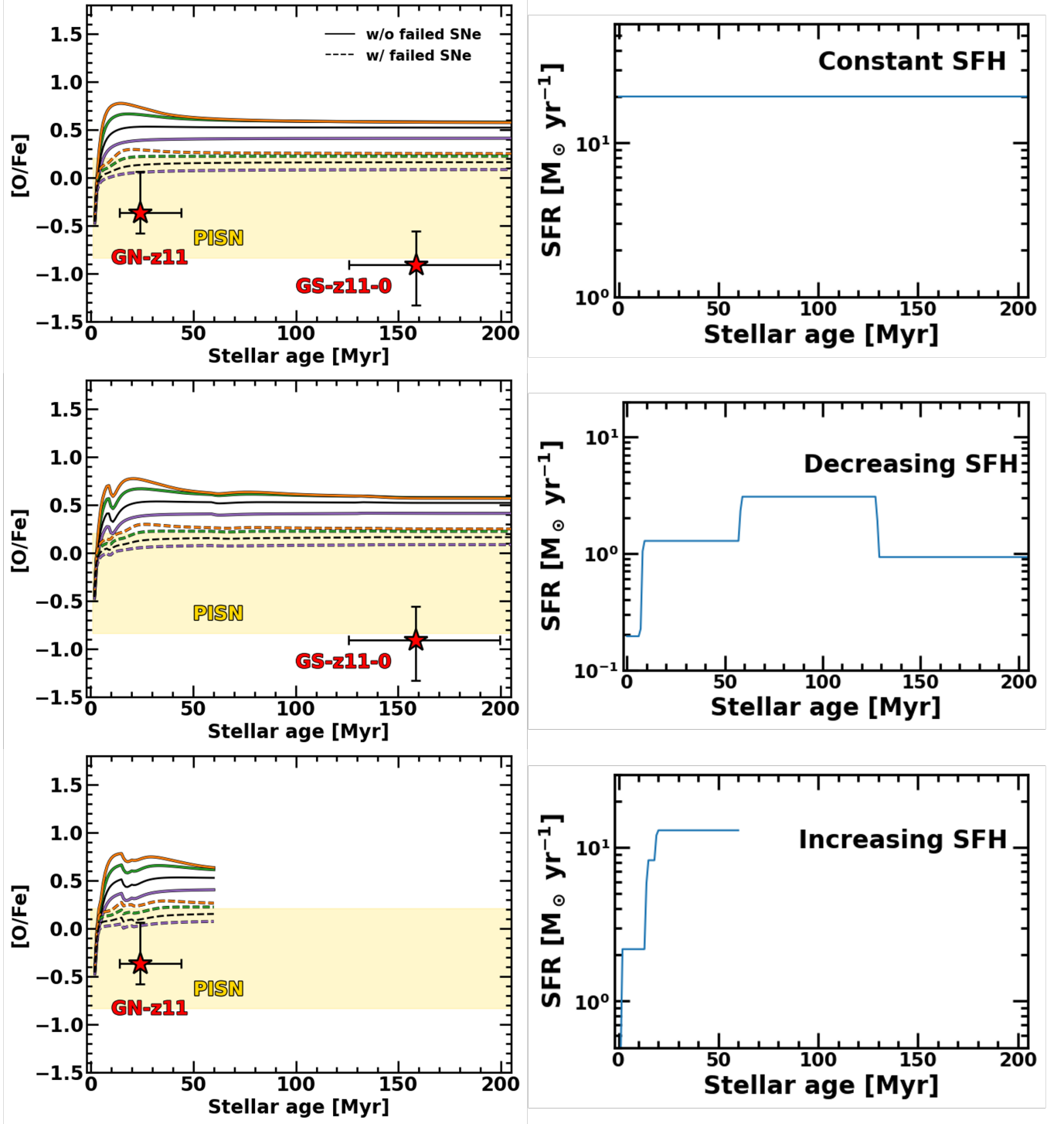


Figure 15. Comparison of the observed abundance ratios with the PISN models. The top, middle, and bottom panels show $[O/Fe]$ as a function of stellar age (left) with our PISN models constructed under the assumption of the constant star formation history (SFH), decreasing SFH (Hainline et al. 2024), and increasing SFH (Tacchella et al. 2023) (right), respectively. The red star symbols represent the measurements of GS-z11-0 and GN-z11 in this work and literature (Hainline et al. 2024; Tacchella et al. 2023). The purple, black, green, and orange lines indicate the PISN models with the top-heavy, Salpeter (1955), Kroupa et al. (1993), and top-light IMFs, respectively. The solid and dashed lines denote the PISN models without and with failed SNe, respectively. The yellow-shaded regions present the yield models of PISNe (Takahashi et al. 2018).

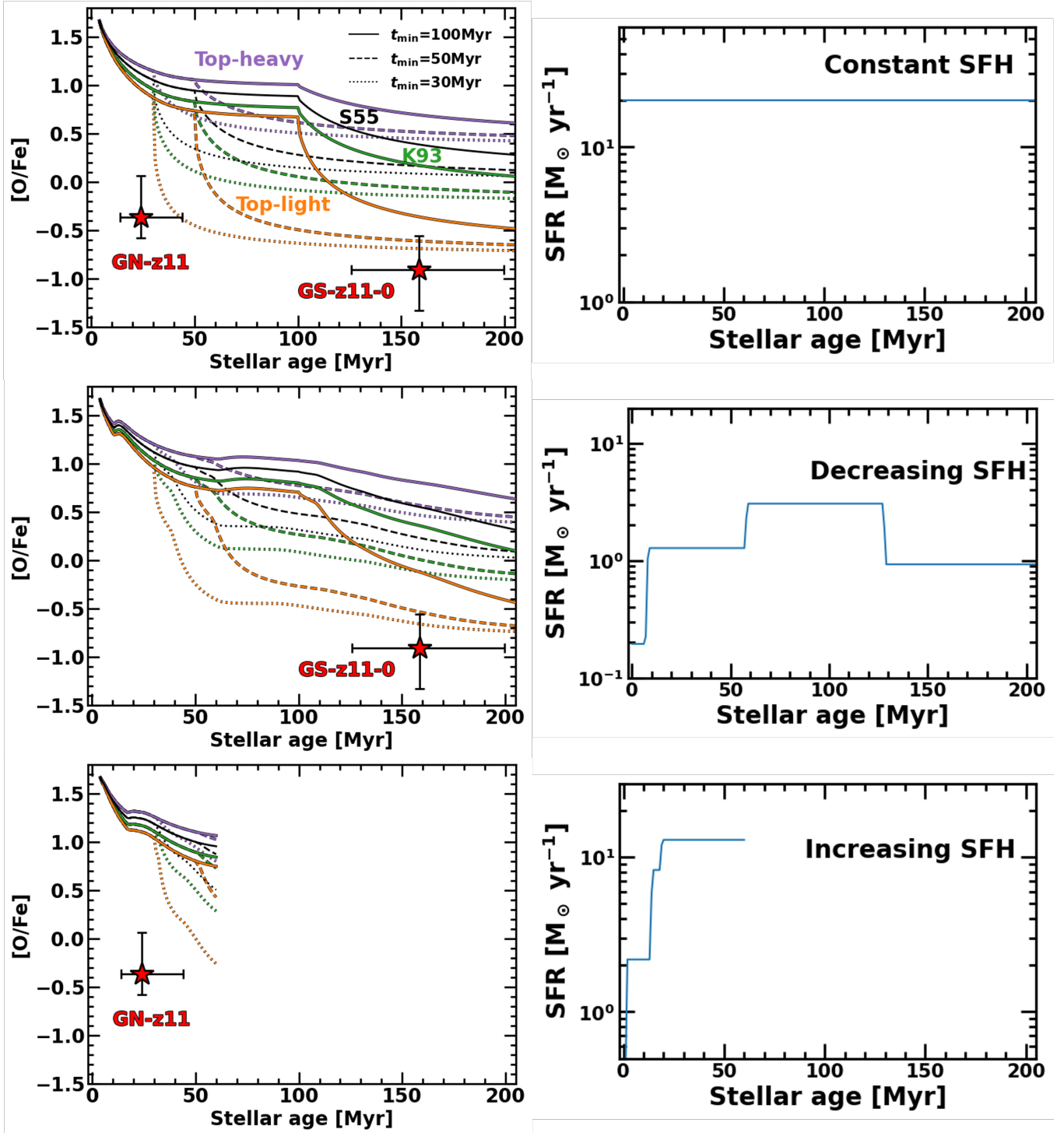


Figure 16. Same as Figure 15, but for the SN Ia models. The solid, dashed, and dotted lines present our SN Ia models with the delay times of $t_{\min} = 100$ Myr, 50 Myr, and 30 Myr, respectively.

PISNe or BrHNe may be likely causes. In summary, the star formation history has minor effects on our results.

We discuss the star formation in the early galaxy with the Fe enhancement based on the comparison with the PISN and SN Ia models. To explain the observed low $[\text{O}/\text{Fe}]$ ratios, it is necessary both to produce iron by PISNe/BrHNe/SNe Ia and to suppress the oxygen enhancement by reducing the contribution from CCSNe. Comparison with the PISNe models suggests that the observed Fe enhancement may be caused by only PISNe or BrHNe. This unusual condition can be interpreted as follows. Under the metal-poor environments in the early epoch of the Universe, massive stars are expected to be predominant based on the hydrodynamical simulations (e.g., Hirano et al. 2014, 2015; Chon et al. 2021). If only massive stars with $M > 140 M_{\odot}$ form as the first generation stars and cause PISNe, Fe-enhanced gas is produced. Alternatively, massive stars ($M \gtrsim 30 M_{\odot}$) in the first generation cause not CCSNe but BrHNe, which also results in the Fe enhancements of the gas. The second generation stars then form from the gas, for which we can observe the low $[\text{O}/\text{Fe}]$ ratios. Actually, this kind of dual bursty star formation scenario is suggested to explain the abundance ratios of high- z galaxies (Kobayashi & Ferrara 2024). For GN-z11, the stellar age of the point source is smaller than that of the extended component, as described above. This suggests a younger starburst in a central, compact region, which may support the dual burst scenario.

The comparison with the SN Ia models suggests that the short delay time and top-light IMF are required to explain the observed low $[\text{O}/\text{Fe}]$ ratios. The short delay time may be accomplished by the fast gas accretion for single degenerate systems or fast white dwarf merger for double degenerate systems in the dense star formation region, which is suggested by the compact morphologies of GS-z11-0 and GN-z11 with the half-light radii of 108 pc and 55 pc, respectively (Ono et al. 2025). The top-light IMF contrasts with the predominant formation of massive stars expected in the early epoch of the Universe as described above. One possibility is that hydrogen deuteride (HD) radiation, which is a more efficient coolant for star-forming gas, plays a greater role than the standard coolant of molecular hydrogen (H_2), resulting in fewer massive stars (e.g., Hirano et al. 2014; Nishijima et al. 2024). In the SNe Ia case, we note that the metallicity dependence of the delay time distribution for the single degenerate systems is suggested (e.g., Kobayashi & Nomoto 2009). For the accreting white dwarf, the optically thick winds, which regulate the mass accretion rate, are mainly due to the opacity of iron and can be critical to cause SNe Ia (e.g., Hachisu et al. 1996,

1999; Kobayashi et al. 1998). Based on the results of Kobayashi & Nomoto (2009), short delay time for the single degenerate systems requires the high iron abundances ($[\text{Fe}/\text{H}] \gtrsim -1$) for the progenitor of the SNe Ia. However, it may not be possible to realize both to form the iron-rich ($[\text{Fe}/\text{H}] \gtrsim -1$) progenitors and to cause SNe Ia in the epoch as early as $z \sim 10$. This implies that if the Fe enhancement is caused by SNe Ia with short delay time, the progenitors of SNe Ia may be the double-degenerate systems. For iron enrichment by SNe Ia, it is worth to compare with the stars in the MW and Sculptor galaxies. In the $[\text{Fe}/\text{H}]-[\text{O}/\text{Fe}]$ plot (Figure 11), our high- z galaxies are on a different sequence from the MW stars, but appear to be on the same sequence as the metal-poor stars in the Sculptor galaxy. While $[\text{O}/\text{Fe}]$ of the MW stars begin to decrease at $[\text{Fe}/\text{H}] \sim -1$, that of the stars in the Sculptor galaxy start to decrease at $[\text{Fe}/\text{H}] \sim -2$ (e.g., Tang et al. 2023). This may imply that the high- z galaxies experience a similar Fe enrichment by SNe Ia to the Sculptor galaxy, which is earlier than the MW.

For further exploration of the low $[\text{O}/\text{Fe}]$ ratios in the early galaxies, it is important to examine other elemental abundance ratios. While GS-z11-0 show only a few emission lines (Hainline et al. 2024), many emission lines are detected for GN-z11 (Bunker et al. 2023) (see Figure 2). In particular, a nitrogen-enhanced ratio of $[\text{N}/\text{O}] > 0.61$ for GN-z11 (Cameron et al. 2023) is also puzzling. To accomplish the high $[\text{N}/\text{O}]$ ratio, it is required to suppress oxygen enhancement as well as in the case of the low $[\text{O}/\text{Fe}]$ ratios. One possible scenario to explain both the high $[\text{N}/\text{O}]$ and low $[\text{O}/\text{Fe}]$ ratios is the dual starbursts (e.g., Kobayashi & Ferrara 2024; Nakane et al. 2024). One of the other possible scenarios is the chemically different wind (e.g., Rizzuti et al. 2024). In this scenario, elements such as nitrogen produced by low/intermediate mass stars or iron originating in SNe Ia, all formed in isolation, are less ejected from the galaxy relative to α -elements (e.g., oxygen) selectively ejected by CCSNe, which are clustered together. The high $[\text{N}/\text{O}]$ ratios of GN-z11 and other high- z galaxies can be explained by the differential winds in Rizzuti et al. (2024). For the low $[\text{O}/\text{Fe}]$ ratios, we may need to reconcile the weak winds from isolated SNe Ia with short delay time, which requires fast gas accretion/white dwarf merger, possibly triggered in the dense star formation. In any cases, all of PISNe, BrHNe, and SNe Ia have possibility to reproduce the observed low $[\text{O}/\text{Fe}]$ and high $[\text{N}/\text{O}]$ ratios. To distinguish the origins of the low $[\text{O}/\text{Fe}]$ ratios, it is necessary to use intermediate-mass elements, such as S and Ar, demonstrated in the recent

studies (e.g., Watanabe et al. 2024; Leung & Nomoto 2024).

5. SUMMARY

In this paper, we present our measurements of Fe abundances for 6 galaxies at $9.3 < z < 12.3$ with $-22 < M_{UV} < -19$ selected based on the high S/N spectra obtained from multiple JWST/NIRSpec programs. To measure the iron abundances of $[\text{Fe}/\text{H}]$, we fit the observed spectra with the stellar model spectra in the rest-frame UV wavelength ranges with stellar Fe absorption lines, carefully masking out the other emission and absorption lines. For GN-z11, we also conduct spectral fitting with the AGN models in the case where the UV continuum is dominated by the AGN radiation. Combined with oxygen abundance measurements from emission lines, we obtain $[\text{O}/\text{Fe}]$ ratios. Our major findings are summarized below:

1. We obtain $[\text{Fe}/\text{H}]$ values for 4 galaxies and the 3σ upper limits for 2 galaxies. From $[\text{O}/\text{Fe}]$ measurements, we find that majority of (4 out of 6) galaxies are consistent with iron-poor abundance ratios of $[\text{O}/\text{Fe}] \gtrsim 0$ while that 2 out of 6 galaxies show Fe enhancements (i.e., low $[\text{O}/\text{Fe}]$ values) of $[\text{O}/\text{Fe}] = -0.91^{+0.35}_{-0.42}$ and $-0.37^{+0.43}_{-0.22}$ ($-1.4 - 0.3$) for GS-z11-0 and GN-z11 in the stellar (AGN) case, respectively.
2. The iron-poor abundance ratios ($[\text{O}/\text{Fe}] \gtrsim 0$) of the 4 galaxies are explained by CCSNe as well as those of the $z \sim 2 - 6$ galaxies. In contrast, the Fe enhancements of GS-z11-0 and GN-z11 require the contribution from theoretical PISNe/BrHNe or SNeIa. To explore the origins of low $[\text{O}/\text{Fe}]$ ratios, we develop the chemical evolution models, incorporating the yields of CCSNe, PISNe, and SNe Ia. By comparing our $[\text{O}/\text{Fe}]$ measurements with the models, we suggest that the Fe enhancements are accomplished by 1) PISNe/BrHNe in the first star formation with little contribution from CC-SNe, or 2) SNe Ia with short delay time ($\sim 30 - 50$ Myr) and a top-light IMF.

ACKNOWLEDGEMENTS

We thank Andrea Ferrara, Hajime Fukushima, Koki Kakiichi, Charlotte Mason, and Hidenobu Yajima for the valuable discussions on this work. This work is based on observations made with the NASA/ESA/CSA James Webb Space Telescope. The data were obtained from the Mikulski Archive for Space Telescopes at the Space Telescope Science Institute, which is operated by the Association of Universities for Research in Astronomy, Inc., under NASA contract NAS 5-03127 for JWST. These observations are associated with programs ERS-1345 and DDT-2750 (CEERS), GTO-1180, 1181, 1210, and GO-3215 (JADES), GO-2561 (UNCOVER), GO-1433, and GO-3073. We acknowledge the CEERS, JADES, UNCOVER, GO-1433, and GO-3073 teams led by Steven L. Finkelstein, Daniel Eisenstein & Nora Lützgendorf, Ivo Labbé & Rachel Bezanson, Dan Coe, and Marco Castellano, respectively, for developing their observing programs. Part of the data products presented herein were retrieved from the Dawn JWST Archive (DJA). DJA is an initiative of the Cosmic Dawn Center (DAWN), which is funded by the Danish National Research Foundation under grant DNR140. This publication is based upon work supported by the World Premier International Research Center Initiative (WPI Initiative), MEXT, Japan, and KAKENHI (20H00180, 21H04467) through Japan Society for the Promotion of Science. Y.I. is supported by JSPS KAKENHI Grant No. 24KJ0202. K.N. is supported by JSPS KAKENHI Grant No. 20K04024, 21H044pp, and 23K03452. This work was supported by the joint research program of the Institute for Cosmic Ray Research (ICRR), the University of Tokyo.

Software: NumPy (Harris et al. 2020), matplotlib (Hunter 2007), SciPy (Virtanen et al. 2020), Astropy (Astropy Collaboration et al. 2013, 2018, 2022), emcee (Foreman-Mackey et al. 2013), BPASS v2.2.1 (Eldridge et al. 2017; Stanway & Eldridge 2018), and CLOUDY v23.01 (Ferland et al. 1998; Gunasekera et al. 2023).

REFERENCES

- Abdurro’uf, Larson, R. L., Coe, D., et al. 2024, ApJ, 973, 47, doi: [10.3847/1538-4357/ad6001](https://doi.org/10.3847/1538-4357/ad6001)
- Akaike, H. 1973, Information Theory and an Extension of the Maximum Likelihood Principle (New York, NY: Springer New York), 199–213
- Álvarez-Márquez, J., Crespo Gómez, A., Colina, L., et al. 2024, arXiv e-prints, arXiv:2412.12826, doi: [10.48550/arXiv.2412.12826](https://doi.org/10.48550/arXiv.2412.12826)
- Amarsi, A. M., Nissen, P. E., & Skúladóttir, Á. 2019, A&A, 630, A104, doi: [10.1051/0004-6361/201936265](https://doi.org/10.1051/0004-6361/201936265)
- Arellano-Córdova, K. Z., Berg, D. A., Chisholm, J., et al. 2022, ApJL, 940, L23, doi: [10.3847/2041-8213/ac9ab2](https://doi.org/10.3847/2041-8213/ac9ab2)

- Arrabal Haro, P., Dickinson, M., Finkelstein, S. L., et al. 2023a, *ApJL*, 951, L22, doi: [10.3847/2041-8213/acdd54](https://doi.org/10.3847/2041-8213/acdd54)
- . 2023b, *Nature*, 622, 707, doi: [10.1038/s41586-023-06521-7](https://doi.org/10.1038/s41586-023-06521-7)
- Asplund, M., Amarsi, A. M., & Grevesse, N. 2021, *A&A*, 653, A141, doi: [10.1051/0004-6361/202140445](https://doi.org/10.1051/0004-6361/202140445)
- Astropy Collaboration, Robitaille, T. P., Tollerud, E. J., et al. 2013, *A&A*, 558, A33, doi: [10.1051/0004-6361/201322068](https://doi.org/10.1051/0004-6361/201322068)
- Astropy Collaboration, Price-Whelan, A. M., Sipőcz, B. M., et al. 2018, *AJ*, 156, 123, doi: [10.3847/1538-3881/aabc4f](https://doi.org/10.3847/1538-3881/aabc4f)
- Astropy Collaboration, Price-Whelan, A. M., Lim, P. L., et al. 2022, *ApJ*, 935, 167, doi: [10.3847/1538-4357/ac7c74](https://doi.org/10.3847/1538-4357/ac7c74)
- Baldwin, J. A. 1977, *ApJ*, 214, 679, doi: [10.1086/155294](https://doi.org/10.1086/155294)
- Baldwin, J. A., Burke, W. L., Gaskell, C. M., & Wampler, E. J. 1978, *Nature*, 273, 431, doi: [10.1038/273431a0](https://doi.org/10.1038/273431a0)
- Bensby, T., Yee, J. C., Feltzing, S., et al. 2013, *A&A*, 549, A147, doi: [10.1051/0004-6361/201220678](https://doi.org/10.1051/0004-6361/201220678)
- Bezanson, R., Labbe, I., Whitaker, K. E., et al. 2024, *ApJ*, 974, 92, doi: [10.3847/1538-4357/ad66cf](https://doi.org/10.3847/1538-4357/ad66cf)
- Bogdán, Á., Goulding, A. D., Natarajan, P., et al. 2024, *Nature Astronomy*, 8, 126, doi: [10.1038/s41550-023-02111-9](https://doi.org/10.1038/s41550-023-02111-9)
- Boyett, K., Trenti, M., Leethochawalit, N., et al. 2023, arXiv e-prints, arXiv:2303.00306, doi: [10.48550/arXiv.2303.00306](https://doi.org/10.48550/arXiv.2303.00306)
- Brandt, J. C., Heap, S. R., Beaver, E. A., et al. 1998, *AJ*, 116, 941, doi: [10.1086/300446](https://doi.org/10.1086/300446)
- Bunker, A. J., Saxena, A., Cameron, A. J., et al. 2023, *A&A*, 677, A88, doi: [10.1051/0004-6361/202346159](https://doi.org/10.1051/0004-6361/202346159)
- Bunker, A. J., Cameron, A. J., Curtis-Lake, E., et al. 2024, *A&A*, 690, A288, doi: [10.1051/0004-6361/202347094](https://doi.org/10.1051/0004-6361/202347094)
- Calzetti, D., Armus, L., Bohlin, R. C., et al. 2000, *ApJ*, 533, 682, doi: [10.1086/308692](https://doi.org/10.1086/308692)
- Cameron, A. J., Katz, H., Rey, M. P., & Saxena, A. 2023, *MNRAS*, 523, 3516, doi: [10.1093/mnras/stad1579](https://doi.org/10.1093/mnras/stad1579)
- Carretta, E., Bragaglia, A., Gratton, R. G., et al. 2010, *A&A*, 516, A55, doi: [10.1051/0004-6361/200913451](https://doi.org/10.1051/0004-6361/200913451)
- Carretta, E., Gratton, R. G., Lucatello, S., Bragaglia, A., & Bonifacio, P. 2005, *A&A*, 433, 597, doi: [10.1051/0004-6361:20041892](https://doi.org/10.1051/0004-6361:20041892)
- Castellano, M., Napolitano, L., Fontana, A., et al. 2024, *ApJ*, 972, 143, doi: [10.3847/1538-4357/ad5f88](https://doi.org/10.3847/1538-4357/ad5f88)
- Chen, X., Hu, L., & Wang, L. 2021, *ApJ*, 922, 15, doi: [10.3847/1538-4357/ac178d](https://doi.org/10.3847/1538-4357/ac178d)
- Chon, S., Omukai, K., & Schneider, R. 2021, *MNRAS*, 508, 4175, doi: [10.1093/mnras/stab2497](https://doi.org/10.1093/mnras/stab2497)
- Cullen, F., McLure, R. J., Dunlop, J. S., et al. 2019, *MNRAS*, 487, 2038, doi: [10.1093/mnras/stz1402](https://doi.org/10.1093/mnras/stz1402)
- Cullen, F., Shapley, A. E., McLure, R. J., et al. 2021, *MNRAS*, 505, 903, doi: [10.1093/mnras/stab1340](https://doi.org/10.1093/mnras/stab1340)
- Curti, M., Cresci, G., Mannucci, F., et al. 2017, *MNRAS*, 465, 1384, doi: [10.1093/mnras/stw2766](https://doi.org/10.1093/mnras/stw2766)
- Curti, M., Mannucci, F., Cresci, G., & Maiolino, R. 2020, *MNRAS*, 491, 944, doi: [10.1093/mnras/stz2910](https://doi.org/10.1093/mnras/stz2910)
- Curti, M., D'Eugenio, F., Carniani, S., et al. 2023, *MNRAS*, 518, 425, doi: [10.1093/mnras/stac2737](https://doi.org/10.1093/mnras/stac2737)
- Curti, M., Witstok, J., Jakobsen, P., et al. 2024, arXiv e-prints, arXiv:2407.02575, doi: [10.48550/arXiv.2407.02575](https://doi.org/10.48550/arXiv.2407.02575)
- De Rosa, G., Decarli, R., Walter, F., et al. 2011, *ApJ*, 739, 56, doi: [10.1088/0004-637X/739/2/56](https://doi.org/10.1088/0004-637X/739/2/56)
- Dean, C. A., & Bruhweiler, F. C. 1985, *ApJS*, 57, 133, doi: [10.1086/190998](https://doi.org/10.1086/190998)
- D'Eugenio, F., Maiolino, R., Carniani, S., et al. 2024a, *A&A*, 689, A152, doi: [10.1051/0004-6361/202348636](https://doi.org/10.1051/0004-6361/202348636)
- D'Eugenio, F., Cameron, A. J., Scholtz, J., et al. 2024b, arXiv e-prints, arXiv:2404.06531, doi: [10.48550/arXiv.2404.06531](https://doi.org/10.48550/arXiv.2404.06531)
- Dietrich, M., Hamann, F., Appenzeller, I., & Vestergaard, M. 2003, *ApJ*, 596, 817, doi: [10.1086/378045](https://doi.org/10.1086/378045)
- Dietrich, M., Hamann, F., Shields, J. C., et al. 2002, *ApJ*, 581, 912, doi: [10.1086/344410](https://doi.org/10.1086/344410)
- Dong, X.-B., Wang, J.-G., Ho, L. C., et al. 2011, *ApJ*, 736, 86, doi: [10.1088/0004-637X/736/2/86](https://doi.org/10.1088/0004-637X/736/2/86)
- Ebinger, K., Curtis, S., Ghosh, S., et al. 2020, *ApJ*, 888, 91, doi: [10.3847/1538-4357/ab5dcb](https://doi.org/10.3847/1538-4357/ab5dcb)
- Eisenstein, D. J., Willott, C., Albers, S., et al. 2023a, arXiv e-prints, arXiv:2306.02465, doi: [10.48550/arXiv.2306.02465](https://doi.org/10.48550/arXiv.2306.02465)
- Eisenstein, D. J., Johnson, B. D., Robertson, B., et al. 2023b, arXiv e-prints, arXiv:2310.12340, doi: [10.48550/arXiv.2310.12340](https://doi.org/10.48550/arXiv.2310.12340)
- Eldridge, J. J., Stanway, E. R., Xiao, L., et al. 2017, *PASA*, 34, e058, doi: [10.1017/pasa.2017.51](https://doi.org/10.1017/pasa.2017.51)
- Ferland, G. J., Korista, K. T., Verner, D. A., et al. 1998, *PASP*, 110, 761, doi: [10.1086/316190](https://doi.org/10.1086/316190)
- Finkelstein, S. L., Bagley, M. B., Ferguson, H. C., et al. 2023, *ApJL*, 946, L13, doi: [10.3847/2041-8213/acade4](https://doi.org/10.3847/2041-8213/acade4)
- Foreman-Mackey, D., Hogg, D. W., Lang, D., & Goodman, J. 2013, *PASP*, 125, 306, doi: [10.1086/670067](https://doi.org/10.1086/670067)
- Fujimoto, S., Arrabal Haro, P., Dickinson, M., et al. 2023, *ApJL*, 949, L25, doi: [10.3847/2041-8213/acd2d9](https://doi.org/10.3847/2041-8213/acd2d9)
- Gardner, J. P., Mather, J. C., Abbott, R., et al. 2023, *PASP*, 135, 068001, doi: [10.1088/1538-3873/acd1b5](https://doi.org/10.1088/1538-3873/acd1b5)
- Goulding, A. D., Greene, J. E., Setton, D. J., et al. 2023, *ApJL*, 955, L24, doi: [10.3847/2041-8213/acf7c5](https://doi.org/10.3847/2041-8213/acf7c5)
- Grandi, S. A. 1982, *ApJ*, 255, 25, doi: [10.1086/159799](https://doi.org/10.1086/159799)

- Gunasekera, C. M., van Hoof, P. A. M., Chatzikos, M., & Ferland, G. J. 2023, *Research Notes of the American Astronomical Society*, 7, 246, doi: [10.3847/2515-5172/ad0e75](https://doi.org/10.3847/2515-5172/ad0e75)
- Hachisu, I., Kato, M., & Nomoto, K. 1996, *ApJL*, 470, L97, doi: [10.1086/310303](https://doi.org/10.1086/310303)
- . 1999, *ApJ*, 522, 487, doi: [10.1086/307608](https://doi.org/10.1086/307608)
- Hainline, K. N., D'Eugenio, F., Jakobsen, P., et al. 2024, arXiv e-prints, arXiv:2404.04325, doi: [10.48550/arXiv.2404.04325](https://doi.org/10.48550/arXiv.2404.04325)
- Harikane, Y., Laporte, N., Ellis, R. S., & Matsuoka, Y. 2020, *ApJ*, 902, 117, doi: [10.3847/1538-4357/abb597](https://doi.org/10.3847/1538-4357/abb597)
- Harikane, Y., Nakajima, K., Ouchi, M., et al. 2024, *ApJ*, 960, 56, doi: [10.3847/1538-4357/ad0b7e](https://doi.org/10.3847/1538-4357/ad0b7e)
- Harris, C. R., Millman, K. J., van der Walt, S. J., et al. 2020, *Nature*, 585, 357, doi: [10.1038/s41586-020-2649-2](https://doi.org/10.1038/s41586-020-2649-2)
- Hill, V., Skúladóttir, Á., Tolstoy, E., et al. 2019, *A&A*, 626, A15, doi: [10.1051/0004-6361/201833950](https://doi.org/10.1051/0004-6361/201833950)
- Hirano, S., Hosokawa, T., Yoshida, N., Omukai, K., & Yorke, H. W. 2015, *MNRAS*, 448, 568, doi: [10.1093/mnras/stv044](https://doi.org/10.1093/mnras/stv044)
- Hirano, S., Hosokawa, T., Yoshida, N., et al. 2014, *ApJ*, 781, 60, doi: [10.1088/0004-637X/781/2/60](https://doi.org/10.1088/0004-637X/781/2/60)
- Hsiao, T. Y.-Y., Abdurro'uf, Coe, D., et al. 2023, arXiv e-prints, arXiv:2305.03042, doi: [10.48550/arXiv.2305.03042](https://doi.org/10.48550/arXiv.2305.03042)
- Hsiao, T. Y.-Y., Álvarez-Márquez, J., Coe, D., et al. 2024, *ApJ*, 973, 81, doi: [10.3847/1538-4357/ad6562](https://doi.org/10.3847/1538-4357/ad6562)
- Hunter, J. D. 2007, *Computing in Science & Engineering*, 9, 90, doi: [10.1109/MCSE.2007.55](https://doi.org/10.1109/MCSE.2007.55)
- Inoue, A. K., Shimizu, I., Iwata, I., & Tanaka, M. 2014, *MNRAS*, 442, 1805, doi: [10.1093/mnras/stu936](https://doi.org/10.1093/mnras/stu936)
- Isobe, Y., Ouchi, M., Nakajima, K., et al. 2023a, *ApJ*, 956, 139, doi: [10.3847/1538-4357/acf376](https://doi.org/10.3847/1538-4357/acf376)
- Isobe, Y., Ouchi, M., Suzuki, A., et al. 2022, *ApJ*, 925, 111, doi: [10.3847/1538-4357/ac3509](https://doi.org/10.3847/1538-4357/ac3509)
- Isobe, Y., Ouchi, M., Tominaga, N., et al. 2023b, *ApJ*, 959, 100, doi: [10.3847/1538-4357/ad09be](https://doi.org/10.3847/1538-4357/ad09be)
- Iwamoto, K., Brachwitz, F., Nomoto, K., et al. 1999, *ApJS*, 125, 439, doi: [10.1086/313278](https://doi.org/10.1086/313278)
- Izotov, Y. I., Worseck, G., Schaerer, D., et al. 2018, *MNRAS*, 478, 4851, doi: [10.1093/mnras/sty1378](https://doi.org/10.1093/mnras/sty1378)
- Jakobsen, P., Ferruit, P., Alves de Oliveira, C., et al. 2022, *A&A*, 661, A80, doi: [10.1051/0004-6361/202142663](https://doi.org/10.1051/0004-6361/202142663)
- Ji, X., Übler, H., Maiolino, R., et al. 2024a, *MNRAS*, doi: [10.1093/mnras/stae2375](https://doi.org/10.1093/mnras/stae2375)
- Ji, X., Maiolino, R., Ferland, G., et al. 2024b, arXiv e-prints, arXiv:2405.05772, doi: [10.48550/arXiv.2405.05772](https://doi.org/10.48550/arXiv.2405.05772)
- Jones, G. C., Bunker, A. J., Saxena, A., et al. 2024, *A&A*, 683, A238, doi: [10.1051/0004-6361/202347099](https://doi.org/10.1051/0004-6361/202347099)
- Kashino, D., Lilly, S. J., Renzini, A., et al. 2022, *ApJ*, 925, 82, doi: [10.3847/1538-4357/ac399e](https://doi.org/10.3847/1538-4357/ac399e)
- Kobayashi, C., & Ferrara, A. 2024, *ApJL*, 962, L6, doi: [10.3847/2041-8213/ad1de1](https://doi.org/10.3847/2041-8213/ad1de1)
- Kobayashi, C., & Nomoto, K. 2009, *ApJ*, 707, 1466, doi: [10.1088/0004-637X/707/2/1466](https://doi.org/10.1088/0004-637X/707/2/1466)
- Kobayashi, C., Tsujimoto, T., Nomoto, K., Hachisu, I., & Kato, M. 1998, *ApJL*, 503, L155, doi: [10.1086/311556](https://doi.org/10.1086/311556)
- Kojima, T., Ouchi, M., Rauch, M., et al. 2020, *ApJ*, 898, 142, doi: [10.3847/1538-4357/aba047](https://doi.org/10.3847/1538-4357/aba047)
- . 2021, *ApJ*, 913, 22, doi: [10.3847/1538-4357/abec3d](https://doi.org/10.3847/1538-4357/abec3d)
- Kroupa, P., Tout, C. A., & Gilmore, G. 1993, *MNRAS*, 262, 545, doi: [10.1093/mnras/262.3.545](https://doi.org/10.1093/mnras/262.3.545)
- Kurk, J. D., Walter, F., Fan, X., et al. 2007, *ApJ*, 669, 32, doi: [10.1086/521596](https://doi.org/10.1086/521596)
- Laor, A., Bahcall, J. N., Jannuzi, B. T., Schneider, D. P., & Green, R. F. 1995, *ApJS*, 99, 1, doi: [10.1086/192177](https://doi.org/10.1086/192177)
- Lecureur, A., Hill, V., Zoccali, M., et al. 2007, *A&A*, 465, 799, doi: [10.1051/0004-6361:20066036](https://doi.org/10.1051/0004-6361:20066036)
- Leung, S.-C., & Nomoto, K. 2024, *ApJ*, 974, 310, doi: [10.3847/1538-4357/ad6ddb](https://doi.org/10.3847/1538-4357/ad6ddb)
- Maiolino, R., & Mannucci, F. 2019, *A&A Rv*, 27, 3, doi: [10.1007/s00159-018-0112-2](https://doi.org/10.1007/s00159-018-0112-2)
- Maiolino, R., Scholtz, J., Witstok, J., et al. 2024, *Nature*, 627, 59, doi: [10.1038/s41586-024-07052-5](https://doi.org/10.1038/s41586-024-07052-5)
- Maoz, D., & Graur, O. 2017, *ApJ*, 848, 25, doi: [10.3847/1538-4357/aa8b6e](https://doi.org/10.3847/1538-4357/aa8b6e)
- Maoz, D., Mannucci, F., & Nelemans, G. 2014, *ARA&A*, 52, 107, doi: [10.1146/annurev-astro-082812-141031](https://doi.org/10.1146/annurev-astro-082812-141031)
- Mazzucchelli, C., Bañados, E., Venemans, B. P., et al. 2017, *ApJ*, 849, 91, doi: [10.3847/1538-4357/aa9185](https://doi.org/10.3847/1538-4357/aa9185)
- Meléndez, J., Barbuy, B., Bica, E., et al. 2003, *A&A*, 411, 417, doi: [10.1051/0004-6361:20031357](https://doi.org/10.1051/0004-6361:20031357)
- Nakajima, K., Ouchi, M., Isobe, Y., et al. 2023, *ApJS*, 269, 33, doi: [10.3847/1538-4365/acd556](https://doi.org/10.3847/1538-4365/acd556)
- Nakajima, K., Ouchi, M., Xu, Y., et al. 2022, *ApJS*, 262, 3, doi: [10.3847/1538-4365/ac7710](https://doi.org/10.3847/1538-4365/ac7710)
- Nakane, M., Ouchi, M., Nakajima, K., et al. 2024, *ApJ*, 976, 122, doi: [10.3847/1538-4357/ad84e810.1134/S1063773708080045](https://doi.org/10.3847/1538-4357/ad84e810.1134/S1063773708080045)
- Napolitano, L., Castellano, M., Pentericci, L., et al. 2024, arXiv e-prints, arXiv:2410.10967, doi: [10.48550/arXiv.2410.10967](https://doi.org/10.48550/arXiv.2410.10967)
- Nishijima, S., Hirano, S., & Umeda, H. 2024, *ApJ*, 965, 141, doi: [10.3847/1538-4357/ad2fc9](https://doi.org/10.3847/1538-4357/ad2fc9)
- Nomoto, K., Kobayashi, C., & Tominaga, N. 2013, *ARA&A*, 51, 457, doi: [10.1146/annurev-astro-082812-140956](https://doi.org/10.1146/annurev-astro-082812-140956)

- Nomoto, K., Maeda, K., Mazzali, P. A., et al. 2004, in *Astrophysics and Space Science Library*, Vol. 302, Astrophysics and Space Science Library, ed. C. L. Fryer, 277–325, doi: [10.1007/978-0-306-48599-2_10](https://doi.org/10.1007/978-0-306-48599-2_10)
- Nomoto, K., Thielemann, F. K., & Yokoi, K. 1984, *ApJ*, 286, 644, doi: [10.1086/162639](https://doi.org/10.1086/162639)
- Oke, J. B., & Gunn, J. E. 1983, *ApJ*, 266, 713, doi: [10.1086/160817](https://doi.org/10.1086/160817)
- Ono, Y., Ouchi, M., Harikane, Y., et al. 2025, arXiv e-prints, arXiv:2502.08885, <https://arxiv.org/abs/2502.08885>
- Onoue, M., Bañados, E., Mazzucchelli, C., et al. 2020, *ApJ*, 898, 105, doi: [10.3847/1538-4357/aba193](https://doi.org/10.3847/1538-4357/aba193)
- Padovani, P., & Matteucci, F. 1993, *ApJ*, 416, 26, doi: [10.1086/173212](https://doi.org/10.1086/173212)
- Pasquini, L., Ecuivillon, A., Bonifacio, P., & Wolff, B. 2008, *A&A*, 489, 315, doi: [10.1051/0004-6361:200809963](https://doi.org/10.1051/0004-6361:200809963)
- Price, S. H., Bezanson, R., Labbe, I., et al. 2024, arXiv e-prints, arXiv:2408.03920, doi: [10.48550/arXiv.2408.03920](https://doi.org/10.48550/arXiv.2408.03920)
- Rix, S. A., Pettini, M., Leitherer, C., et al. 2004, *ApJ*, 615, 98, doi: [10.1086/424031](https://doi.org/10.1086/424031)
- Rizzuti, F., Matteucci, F., Molaro, P., Cescutti, G., & Maiolino, R. 2024, arXiv e-prints, arXiv:2412.05363, doi: [10.48550/arXiv.2412.05363](https://doi.org/10.48550/arXiv.2412.05363)
- Rodney, S. A., Riess, A. G., Strolger, L.-G., et al. 2014, *AJ*, 148, 13, doi: [10.1088/0004-6256/148/1/13](https://doi.org/10.1088/0004-6256/148/1/13)
- Salpeter, E. E. 1955, *ApJ*, 121, 161, doi: [10.1086/145971](https://doi.org/10.1086/145971)
- Sameshima, H., Yoshii, Y., & Kawara, K. 2017, *ApJ*, 834, 203, doi: [10.3847/1538-4357/834/2/203](https://doi.org/10.3847/1538-4357/834/2/203)
- Sameshima, H., Yoshii, Y., Matsunaga, N., et al. 2020, *ApJ*, 904, 162, doi: [10.3847/1538-4357/abc33b](https://doi.org/10.3847/1538-4357/abc33b)
- Sanders, R. L., Shapley, A. E., Topping, M. W., Reddy, N. A., & Brammer, G. B. 2024, *ApJ*, 962, 24, doi: [10.3847/1538-4357/ad15fc](https://doi.org/10.3847/1538-4357/ad15fc)
- Shin, J., Nagao, T., Woo, J.-H., & Le, H. A. N. 2019, *ApJ*, 874, 22, doi: [10.3847/1538-4357/ab05da](https://doi.org/10.3847/1538-4357/ab05da)
- Stanway, E. R., & Eldridge, J. J. 2018, *MNRAS*, 479, 75, doi: [10.1093/mnras/sty1353](https://doi.org/10.1093/mnras/sty1353)
- Steidel, C. C., Strom, A. L., Pettini, M., et al. 2016, *ApJ*, 826, 159, doi: [10.3847/0004-637X/826/2/159](https://doi.org/10.3847/0004-637X/826/2/159)
- Suzuki, A., & Maeda, K. 2018, *ApJ*, 852, 101, doi: [10.3847/1538-4357/aaa024](https://doi.org/10.3847/1538-4357/aaa024)
- Tacchella, S., Eisenstein, D. J., Hainline, K., et al. 2023, *ApJ*, 952, 74, doi: [10.3847/1538-4357/acdbc6](https://doi.org/10.3847/1538-4357/acdbc6)
- Tacchella, S., McClymont, W., Scholtz, J., et al. 2024, arXiv e-prints, arXiv:2404.02194, doi: [10.48550/arXiv.2404.02194](https://doi.org/10.48550/arXiv.2404.02194)
- Takahashi, K., Yoshida, T., & Umeda, H. 2018, *ApJ*, 857, 111, doi: [10.3847/1538-4357/aab95f](https://doi.org/10.3847/1538-4357/aab95f)
- Tang, B., Zhang, J., Yan, Z., et al. 2023, *A&A*, 669, A125, doi: [10.1051/0004-6361/202244052](https://doi.org/10.1051/0004-6361/202244052)
- Tegmark, M., Silk, J., Rees, M. J., et al. 1997, *ApJ*, 474, 1, doi: [10.1086/303434](https://doi.org/10.1086/303434)
- Topping, M. W., Stark, D. P., Senchyna, P., et al. 2024a, *MNRAS*, 529, 3301, doi: [10.1093/mnras/stae682](https://doi.org/10.1093/mnras/stae682)
- . 2024b, arXiv e-prints, arXiv:2407.19009, doi: [10.48550/arXiv.2407.19009](https://doi.org/10.48550/arXiv.2407.19009)
- Topping, M. W., Sanders, R. L., Shapley, A. E., et al. 2025, arXiv e-prints, arXiv:2502.08712, doi: [10.48550/arXiv.2502.08712](https://doi.org/10.48550/arXiv.2502.08712)
- Totani, T., Morokuma, T., Oda, T., Doi, M., & Yasuda, N. 2008, *PASJ*, 60, 1327, doi: [10.1093/pasj/60.6.1327](https://doi.org/10.1093/pasj/60.6.1327)
- Tsuzuki, Y., Kawara, K., Yoshii, Y., et al. 2006, *ApJ*, 650, 57, doi: [10.1086/506376](https://doi.org/10.1086/506376)
- Umeda, H., & Nomoto, K. 2008, *ApJ*, 673, 1014, doi: [10.1086/524767](https://doi.org/10.1086/524767)
- Valenti, E., Origlia, L., & Rich, R. M. 2011, *MNRAS*, 414, 2690, doi: [10.1111/j.1365-2966.2011.18580.x](https://doi.org/10.1111/j.1365-2966.2011.18580.x)
- Virtanen, P., Gommers, R., Oliphant, T. E., et al. 2020, *Nature Methods*, 17, 261, doi: [10.1038/s41592-019-0686-2](https://doi.org/10.1038/s41592-019-0686-2)
- Watanabe, K., Ouchi, M., Nakajima, K., et al. 2024, *ApJ*, 962, 50, doi: [10.3847/1538-4357/ad13ff](https://doi.org/10.3847/1538-4357/ad13ff)
- Watanabe, S. 2010, *Journal of Machine Learning Research*, 11, 3571. <http://jmlr.org/papers/v11/watanabe10a.html>
- Yong, D., Grundahl, F., Johnson, J. A., & Asplund, M. 2008, *ApJ*, 684, 1159, doi: [10.1086/590658](https://doi.org/10.1086/590658)
- Yong, D., Grundahl, F., Nissen, P. E., Jensen, H. R., & Lambert, D. L. 2005, *A&A*, 438, 875, doi: [10.1051/0004-6361:20052916](https://doi.org/10.1051/0004-6361:20052916)
- Yoshii, Y., Sameshima, H., Tsujimoto, T., et al. 2022, *ApJ*, 937, 61, doi: [10.3847/1538-4357/ac8163](https://doi.org/10.3847/1538-4357/ac8163)
- Zhao, G., Mashonkina, L., Yan, H. L., et al. 2016, *ApJ*, 833, 225, doi: [10.3847/1538-4357/833/2/225](https://doi.org/10.3847/1538-4357/833/2/225)